JGR Atmospheres

RESEARCH ARTICLE
10.1029/2018JD028853

Evaporative Implications of Dry-Air Outbreaks Over the Northern Red Sea

Viviane V. Menezes[1], **J. Thomas Farrar**[1], **and Amy S. Bower**[1]

[1]Department of Physical Oceanography, Woods Hole Oceanographic Institution, Woods Hole, MA, USA

Key Points:
- Relative humidity controls the evaporation during westward events, with the highest evaporation over the Eastern Boundary Current
- Westward wind event frequency consistently increased over the last three decades (1980 to 2015)
- A strong Arabian High favors westward wind events, suggesting that these events and the winter Shamal in the Persian Gulf are connected

Supporting Information:
- Supporting Information S1

Correspondence to:
V. V. Menezes,
vmenezes@whoi.edu

Citation:
Menezes, V. V., Farrar, J. T., & Bower, A. S. (2019). Evaporative implications of dry-air outbreaks over the northern Red Sea. *Journal of Geophysical Research: Atmospheres*, *124*, 4829–4861. https://doi.org/10.1029/2018JD028853

Received 18 APR 2018
Accepted 19 MAR 2019
Accepted article online 1 APR 2019
Published online 2 MAY 2019

Author Contributions
Conceptualization: Viviane V. Menezes, J. Thomas Farrar, Amy S. Bower
Data curation: J. Thomas Farrar
Funding Acquisition: J. Thomas Farrar, Amy S. Bower
Methodology: Viviane V. Menezes
Software: Viviane V. Menezes
Validation: Viviane V. Menezes
Writing - Original Draft: Viviane V. Menezes
Formal Analysis: Viviane V. Menezes
Investigation: Viviane V. Menezes
Resources: J. Thomas Farrar, Amy S. Bower
Supervision: J. Thomas Farrar, Amy S. Bower
Visualization: Viviane V. Menezes
Writing - review & editing: Viviane V. Menezes, J. Thomas Farrar, Amy S. Bower

Abstract We investigate the impacts of westward wind events on the Red Sea evaporation using the 35-year second Modern-Era Retrospective analysis for Research and Applications reanalysis and a 2-year-long record of in situ observations from a heavily instrumented air-sea interaction mooring. These events are common during boreal winter, and their effects are similar to cold-air outbreaks that occur in midpolar and subpolar latitudes. They cause extreme heat loss from the sea, which is dominated by latent heat fluxes. Different from cold-air outbreaks, the intensified heat loss is due to the low relative humidity as we show through latent heat flux decomposition. Rainfall is negligible during these events, and we refer to them as dry-air outbreaks. We also investigate the general atmospheric circulation pattern that favors their occurrence, which is associated with an intensified Arabian High at the north-central portion of the Arabian Peninsula—a feature that seems to be an extension of the Siberian High. The analyses reveal that the westward winds over the northern Red Sea and the winter Shamal winds in the Persian Gulf are very likely to be part of the same subsynoptic-scale feature. The second Modern-Era Retrospective analysis for Research and Applications reanalysis indicates that the occurrence of westward wind events over the northern Red Sea has grown from 1980 to 2015, especially the frequency of large-scale events, the cause of which is to be investigated. We hypothesize that dry-air outbreaks may induce surface water mass transformation in the surface Red Sea Eastern Boundary Current and could represent a significant process for the oceanic thermohaline-driven overturning circulation.

1. Introduction

The Red Sea, a semienclosed marginal sea of the Indian Ocean located between 12°N and 30°N, is one of the saltiest and warmest water bodies on Earth and a primary source of high salinity waters for the oceanic intermediate layer (e.g., Beal et al., 2000; Han & McCreary, 2001). Intense air-sea interactions characterize the Red Sea, which has one of the highest evaporation rates of the global oceans, with an annual mean of 2.06 ± 0.22 m/year (Bower & Farrar, 2015; Eshel & Heavens, 2007; Sofianos et al., 2002; Tragou et al., 1999).

The intense evaporation drives the basin-scale vertical overturning circulation and contributes to the formation of the Red Sea Overflow Water (RSOW; Bower & Farrar, 2015; Eshel & Naik, 1997; Papadopoulos et al., 2015; Sofianos & Johns, 2003, 2015; Yao, Hoteit, Pratt, Bower, Kohl, et al., 2014; Yao, Hoteit, Pratt, Bower, Zhai, et al., 2014; Zhai, Bower, et al., 2015). This salty water mass escapes to the Indian Ocean, where it can be traced at intermediate depths as far as the Agulhas Current and the Agulhas Return Current at about 40°S (Beal et al., 2000; Roman & Lutjeharms, 2007, 2009; You, 1998). The intense evaporation is also an important source of moisture for the arid Middle-East, influencing the regional hydrological cycle and the precipitation over the adjacent countries (Zolina et al., 2017). Hence, local air-sea interaction processes in the interior of the northern Red Sea can have large-scale impacts in both the atmosphere and ocean.

Evaporation rates increase northward in the Red Sea and are stronger in winter (boreal seasons, hereafter; e.g., Eshel & Heavens, 2007; Papadopoulos et al., 2013; Sofianos et al., 2002; Tragou et al., 1999; Zolina et al., 2017). Based on a unique 2-year-long record of latent surface heat flux derived from in situ observations, Bower and Farrar (2015) describe local evaporation rates at 22°N (central Red Sea) varying from 1 m/year in summer to 3 m/year in winter with peaks exceeding 5 m/year. They found these evaporation peaks associated with surface westward winds that bring dry and relatively cold air and dust from the Arabian Desert over the Red Sea (see also Bower & Farrar, 2015; Jiang et al., 2009; Menezes et al., 2018). Hereafter, we follow the oceanographic convention, that is, to where the winds blow.

The westward wind events have effects similar to cold-air outbreaks that occur in midpolar and subpolar latitudes across the globe (e.g., Dorman et al., 2006; Lee et al., 2005; Marshall et al., 2009; Poulain et al., 2001) and are very distinct from the typical along-axis surface wind regime of the Red Sea (Bower & Farrar, 2015; Jiang et al., 2009; Menezes et al., 2018). As we show in the present work, the intensified heat losses (>600 W/m^2) during westward wind events are due to the low relative humidity of these winds, and because of that, we also refer to these events as dry-air outbreaks. Because these outbreaks can sharply increase surface heat loss and evaporation over the northern Red Sea, they may trigger surface water mass transformation that leads to the RSOW (Bower & Farrar, 2015; Jiang et al., 2009; Kalenderski et al., 2013; Papadopoulos et al., 2013).

Menezes et al. (2018) analyzed the occurrence of the westward wind events in QuikSCAT satellite data and showed that these events are relatively common over the northern Red Sea. They occur in the winter monsoon (October–March), especially in December and January, typically one to three large-scale events (more than 400-km meridional extension) each winter (see, e.g., Figures 5 and 22 in Menezes et al., 2018). In general, the events last from 3 to 8 days, reach speeds up to 13 m/s in QuikSCAT, and have substantial interannual variability (Menezes et al., 2018). They are unmistakably different from other localized orographic-influenced land wind events such as the Mecca-wind event in September 2015 (Dasari et al., 2017).

In a typical event, all the winds over the northern Red Sea are to the west, but there are two regions where the westward winds are more prominent: 22–24°N and 25–26°N (Menezes et al., 2018). These regions are in latitudes correspondent to the broadest mountain gaps on land; gaps in the Red Sea coastal mountains vary from a few kilometers to 50–70 km according to the ETOPO2 global relief data (NGDC, 2006). As shown by Menezes et al. (2018), this is not a coincidence since the desert-origin westward winds pass through the many gaps in the coastal mountains that border the Arabian Peninsula western margin. One of the most significant gaps is in the vicinity of the historical city of Mecca (21°25′ N, 39°49 25′ E). South of Mecca, there are the taller and more compact Asir mountains; north of it, there are the Hijaz mountains, and a separation exists between the two coastal mountain ranges. There are also gaps due to valleys and canyons linked to dry rivers (called wadis), for example, around 26°N; there are gaps related to faults and fractures of the coastal escarpment (e.g., Brown et al., 1989).

It is still under debate why these large-scale westward wind events and associated dry-air outbreaks develop in the northern Red Sea. Jiang et al. (2009) suggest that their occurrence may be due to a local intensification of the Saudi Arabian High by radiative cooling in the Arabian Desert or by the intrusion of cold, continental air flowing out of the Siberian High. Papadopoulos et al. (2013) studied the extreme heat loss over the northern Red Sea and found that the anticyclone over Turkey creates the sea level pressure (SLP) gradients that allow continental, cold and dry air masses to reach the northern Red Sea. This pattern seems to favor the large-scale westward wind events as noted by Bower and Farrar (2015). However, not all extreme sea heat loss days described by Papadopoulos et al. (2013) are due to desert-origin westward winds (see, e.g., their Figure 9).

In the present work, we investigate the general atmospheric circulation pattern (described by SLP) that favors the large-scale surface winds to flow westward over the northern Red Sea in winter and the impacts of these events on the spatial-temporal distribution of the evaporation. We also determine the factors contributing to the sharp latent heat loss (evaporation) observed in dry-air outbreaks by applying a latent heat flux decomposition. The objective is to disentangle the role of variations in sea surface temperature, air-sea temperature difference, relative humidity, and wind speed. Additionally, the relationship between the dry-air outbreaks and the severe heat loss days described by Papadopoulos et al. (2013) is also investigated. This work is part of a research effort aiming to understand the air-sea interaction processes involved in the surface water mass transformation in the northern Red Sea, an essential part of the Red Sea vertical overturning circulation. The investigation is based on the new second Modern-Era Retrospective analysis for Research and Applications (MERRA-2) reanalysis developed by National Aeronautics and Space Administration (Bosilovich et al., 2017) and in situ observations from an air-sea interaction mooring. The mooring was deployed by Woods Hole Oceanographic Institution (WHOI) in collaboration with King Abdullah University of Science and Technology (KAUST) and worked from October 2008 to December 2010 (Bower & Farrar, 2015; Farrar et al., 2009). We start the analyses by comparing MERRA-2 with the in situ observations to show that MERRA-2 captures the westward wind events over the northern Red Sea and their effects

on the evaporation despite its relatively coarse spatial resolution (about 50 km) compared with the Red Sea maximum width (355 km according to, e.g., Bower & Farrar, 2015; Jiang et al., 2009).

The paper is organized as follows: Sections 2 and 3 describe the data sets and the methods, respectively; section 4.1 presents an evaluation of MERRA-2 winds and evaporation rates against in situ observation from the WHOI/KAUST mooring. Section 4.2 describes the northern Red Sea westward wind events in MERRA-2. Section 4.3 focuses on the large-scale SLP patterns associated with these events, section 4.4 on the impacts of these events on the evaporation rates, section 4.5 on the latent heat flux decomposition, and section 4.6 on the relationship between dry-air outbreaks and the severe sea heat losses in winter. Section 4.7 briefly describes the differences between the dry-air outbreaks in the northern Red Sea and the Red Sea Trough (RST) systems, which also occur in the cool season. Section 5 provides a summary and discussion.

2. Data

2.1. MERRA-2

The MERRA-2 atmospheric reanalysis spans from 1980 to the present, but here we focus on a 35-year period between 1980 and 2015. This improved product replaces the original MERRA reanalysis (Bosilovich et al., 2017; Rienecker et al., 2011). MERRA-2 uses the Goddard Earth Observing System Model (GEOS-5), version 5.12.4, configured with a cubed-sphere grid with 72 vertical levels and horizontal resolution of about 50 km (Bosilovich et al., 2016). MERRA-2 assimilates several data types, which include in situ observations of wind and mass fields and measurements from spaceborne observing systems. The satellite-derived winds assimilated in MERRA-2 are atmospheric motion vectors obtained by tracking features in temporally successive satellite images, wind speeds retrieved by Special Sensor Microwave Imager and Special Sensor Microwave Imager Sounder, and ocean surface wind vectors from satellite scatterometers (ERS-1, ERS-2, QuikSCAT, and ASCAT) and derived from the WINDSAT/Coriolis microwave radiometer. McCarty et al. (2016) give a complete description of all data assimilated in MERRA-2.

The MERRA-2 outputs are spatially interpolated to a longitude-latitude grid of $0.625° \times 0.5°$. We use daily-average fields computed from hourly average outputs to smooth the strong diurnal cycle associated with the Red Sea land-sea breezes (Churchill et al., 2014; Davis et al., 2015; Zolina et al., 2017). The following MERRA-2 surface fields are analyzed: evaporation and precipitation rates, latent and sensible heat fluxes, 10-m vector winds, SLP, and air surface temperature. Hereafter, heat fluxes comply with the oceanographic convention: Positive values represent oceanic heat gain.

The primary fields that will be analyzed are evaporation (latent heat flux) and SLP since we aim to understand the impact of dry-air outbreaks on the spatial-temporal distribution of the evaporation and the large-scale atmospheric pattern that favors these events. MERRA-2 has higher spatial and temporal resolutions than the satellite-based OAFlux surface heat fluxes ($1° \times 1°$) used in several studies in the Red Sea (e.g., Abualnaja et al., 2015; Bower & Farrar, 2015; Papadopoulos et al., 2013; Zhai, Bower, et al., 2015) and has a slightly better spatial resolution than the ERA-Interim reanalysis analyzed by, for example, Zolina et al. (2017), who investigated the Red Sea regional hydrological cycle.

In the present work, the MERRA-2 wind fields are used to identify westward wind/dry-air outbreak events in the northern Red Sea. Although the reanalysis wind fields have lower spatial resolution than the wind fields used by Jiang et al. (2009) and Menezes et al. (2018), MERRA-2 captures the overall spatial structure of large-scale westward winds and can be used to identify its occurrence (Figures 1 and S1 in the supporting information). For instance, Figure 1 shows two events in MERRA-2 and the 3-day moving average QuikSCAT wind fields (25-km spatial resolution) produced by Remote Sensing System and analyzed by Menezes et al. (2018). The MERRA-2 winds are slightly weaker when compared with the QuikSCAT winds, but the spatial patterns are similar. For readers interested in the accuracy of QuikSCAT scatterometer winds in the northern Red Sea, we refer to Menezes et al. (2018), who performed a very detailed analysis of QuikSCAT and in situ winds. The latter authors describe correlations between satellite and in situ winds as high as 0.96 (speed) and 0.85 (direction) and a root-mean-square difference (*rmsd*) of 0.72 m/s for winds above 3 m/s. We have also compared MERRA-2 with the downscale 10-km WRF short-period simulation from Jiang et al. (2009) and find that the MERRA-2 wind fields capture the overall pattern including the winds over land, although the wind strength is generally weaker in MERRA-2 (e.g., Figure S1). Moreover, MERRA-2 reproduces relatively well the statistical distribution of coastal QuikSCAT Level 2B winds version

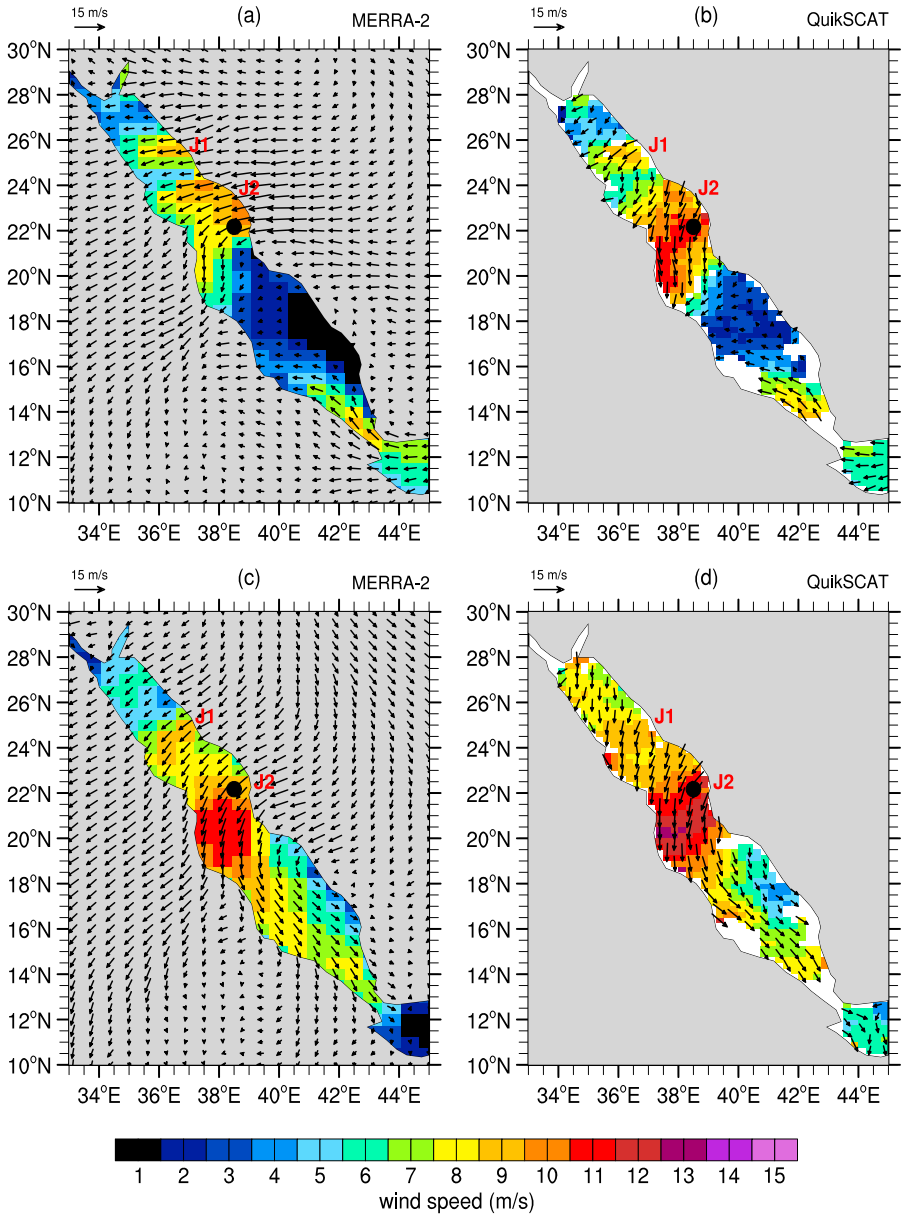

Figure 1. Two examples of wintertime westward wind events over the northern Red Sea in MERRA-2 and QuikSCAT: (a, b) 14–15 January 2009 and (c, d) 27–28 December 2004. Colors indicate the wind speed and vectors the wind direction. Black dot shows the Woods Hole Oceanographic Institution/King Abdullah University of Science and Technology mooring position and J1/J2 labels point to the regions of intensified winds over water. For display purposes, QuikSCAT vectors are shown with a coarsened resolution (approximately 0.5°). Notice QuikSCAT winds are not defined over land. MERRA-2 = second Modern-Era Retrospective analysis for Research and Applications.

4.0 (spatial resolution of 12.5 km; Stiles et al., 2017) between 22°N and 26°N as we show in Figure S2—the region where the westward wind events are most recurrent (Menezes et al., 2018). Hence, MERRA-2 spatial resolution is sufficient to identify westward wind events over the northern Red Sea.

Since MERRA-2 is not entirely independent of QuikSCAT or Weather Research and Forecasting model (WRF), in section 4.1, we compare MERRA-2 winds and evaporation rates to the (nonassimilated) WHOI/KAUST in situ observations at the northern Red Sea. The aim is to verify the accuracy of MERRA-2 winds and evaporation over water. For the comparison, MERRA-2 data between October 2008 and December 2010 from the closest grid point to the mooring location are used (22°N; 38.75°E, 31.99 km of distance between the grid point center and the mooring). In addition, we also compare the MERRA-2 winds with

daily-average in situ winds from coastal-land areas; these coastal-land winds are from a meteorological tower at 22.297°N, 39.0928°E (18 October 2008 to 9 November 2009; WHOI/KAUST partnership) and two long Global Surface Summary of the Day time series available at the National Climatic Data Center/National Oceanic and Atmospheric Administration. These long time series span the MERRA-2 period (1980–2015) and are from the Yenbo (24.144°N; 38.063°E; 7.9 m above mean sea level) and Wejh (26.199°N; 36.476°E; 20.1 m) stations.

2.2. WHOI/KAUST In Situ Mooring Data

Hourly average in situ atmospheric observations from the northern Red Sea at 22.17°N; 38.5°E between 12 October 2008 and 16 December 2010 (796 days) are analyzed (see Figure 1 for the mooring position). These in situ observations are from the WHOI/KAUST mooring, anchored at 693 m depth (Farrar et al., 2009). The mooring was positioned about 55 km (34.1 mi) offshore of Thuwal and northwest of the gap near Mecca, where the Hijaz and Asir Mountains separate (see, e.g., Figures 2a and 2b from Menezes et al., 2018 and Figures 1c and 1d from Jiang et al., 2009). As described by Bower and Farrar (2015) and Menezes et al. (2018), the mooring was in a good location for observing the desert-origin westward winds and thus dry-air outbreaks (Jiang et al., 2009; Menezes et al., 2018). The following variables were measured: surface wind velocity and direction, surface relative humidity and air temperature, barometric pressure, incoming shortwave (incident sunlight) and longwave (infrared) radiations, precipitation, and surface waves. Temperature, salinity, and ocean currents were also measured at depths spanning the full water column (Farrar et al., 2009).

Air-sea fluxes of heat, momentum, and freshwater are calculated using the Coupled Ocean-Atmosphere Response Experiment version 3.0 (COARE-3) bulk algorithm (Fairall et al., 2003). For wind speeds between 5 and 15 m/s, which are typical in the Red Sea (Menezes et al., 2018), there is no significant difference between the COARE-3 and the refined COARE 3.5 algorithms (Edson et al., 2013). Evaporation rates (E) are estimated from the latent heat flux (Q_l) as $E = Q_l/(L_v * \rho_w)$, where L_v is the latent heat of vaporization of liquid water and ρ_w is the density of seawater. We assume $L_v = 2.44 \times 10^6$ J/kg and $\rho_w = 1{,}022.4$ kg/m^3, the same values used in the Indian Ocean RAMA array program (McPhaden et al., 2009). In situ winds were converted to winds at 10-m height under neutral stratification condition through the COARE-3 algorithm. Hereafter, in situ winds refer to 10-m winds. The hourly time series have only 0.3% of missing data, which are due to the replacement of the buoy after the first year of operation. We filled the gaps by linear interpolation and computed daily-average observations to smooth the diurnal cycle.

3. Methods

3.1. Identifying Westward Wind Events Over the Northern Red Sea

We use a definition similar to Menezes et al. (2018) to identify the westward wind events over the northern Red Sea in MERRA-2. The events are defined as the occurrence of persistent winds toward 215–280° (oceanographic convention) over the northern Red Sea eastern boundary. Here the two grid points adjacent to the Arabian Peninsula coastline (about 140-km width) delimit the eastern boundary. Only events that occur during the winter are analyzed since the majority of events are found in this season (Menezes et al., 2018). Hereafter, winter refers to the winter monsoon period (October to March). Sea/land areas are defined based on the ETOPO-2 version 2.2 global relief data set (NGDC, 2006; Smith & Sandwell, 1997), bilinearly interpolated to the MERRA-2 grid. ETOPO-2 contains both ocean bathymetry and land topography data with a horizontal grid resolution of 2 min and is distributed by the National Geophysical Data Center.

One limitation faced by Menezes et al. (2018) to identify the winds coming from the Arabian Desert in QuikSCAT was the ambiguity regarding the wind direction between these desert-origin winds and the westward winds associated with the Red Sea Convergence Zone (RSCZ). The RSCZ is the region of weaker winds where the two opposite-blowing along-axis air streams meet and bend to the west in the middle of the Red Sea (about 18–19°N; e.g., Langodan et al., 2015; Menezes et al., 2018; Pedgley, 1966; Viswanadhapalli et al., 2017; Vojtesak et al., 1991; Zolina et al., 2017). Usually, the RSCZ develops in winter, but the RSCZ-associated westward winds do not come from the desert. The southward winds north of the RSCZ are weak and drier, but south of it, the northward winds are stronger and moister, and light rain showers can be present either side (within 90 km) of the RSCZ (Vojtesak et al., 1991). Thus, the RSCZ-associated westward winds are not as dry as the desert-origin westward winds that cause the dry-air outbreaks. Because satellite scatterometer winds are only defined over water, Menezes et al. (2018) could not separate these two kinds of westward winds near the RSCZ (when this zone existed) based on QuikSCAT data alone. We do not have

this limitation in the present study because MERRA-2 wind fields are also defined over land. To exclude the RSCZ-westward winds, we adopted the following condition: A desert-origin westward wind event occurs at a latitude j if both the median winds over the Red Sea eastern boundary and land are in the range 215° to 280°. The median winds over land are computed from the two land grid points adjacent to the Arabian Peninsula coastline. Similar to Menezes et al. (2018), we use zonal velocity $u = -1$ m/s as the threshold to define the start/end of a dry-air outbreak event at each latitude j.

3.2. Westward Wind Event and Winter Composites

We use composite analyses of SLP and evaporation rates to evaluate the general atmospheric circulation pattern associated with the westward wind/dry-air outbreak events over the northern Red Sea and the effect of these events on the spatial-temporal distribution of evaporation. We form the respective composites by averaging the SLP and evaporation fields associated with westward winds. Because the events have different duration, from one to several days (Menezes et al., 2018), for each identified event (see the previous section), we select the field (SLP/evaporation) from the day in which the westward winds have their maximum meridional extension. We do that to avoid sampling bias caused by long-duration events. Our analyses focus on the composites formed by large-scale events, that is, the ones with westward winds extending for at least half of the northern Red Sea meridional extension (4° of latitude). As a reference, we also form winter composites (October–March) by excluding all fields associated with westward wind events larger than 20% of the northern Red Sea meridional extension (1.6° of latitude). Thus, the westward winds related to the narrow RSCZ (100–180-km meridional extension or less) in the central Red Sea will contribute to the winter composite but not for the westward wind event ones. See Menezes et al. (2018) for a more detailed description of the RSCZ. Surface wind, precipitation, and air temperature composites (westward wind and winter) are also formed using the same technique as above to assist the interpretation.

3.3. Latent Heat Flux Decomposition

Westward wind events are characterized by an abrupt increase in latent heat loss (evaporation; Bower & Farrar, 2015). The sharp increase is caused by a combination of intensified zonal winds carrying dry and relatively cold air. To disentangle the contribution of surface relative humidity, near-surface stability, sea surface temperature, and wind speed, we use a diagnostic latent heat flux decomposition approach similar to Bosilovich et al. (2017), Richter and Xie (2008), and Vimont et al. (2009). We apply it to the in situ observations measured at the WHOI/KAUST mooring. The diagnostic decomposition is based on the standard aerodynamic bulk formula for the latent heat flux (Q_l):

$$Q_l = L_v C_e \rho_a W \left[q_s - q_a\right], \tag{1}$$

where L_v is the latent heat of vaporization of liquid water, C_e is the turbulent exchange coefficient for latent heat flux, ρ_a is the is the near-surface air density, W is the scalar wind speed at near-surface (here 10-m height above the sea surface), q_s is the saturation specific humidity at the air-sea interface, which is a function of sea surface temperature (SST), and q_a is the near-surface saturation specific humidity that depends on the air temperature (T_a) and relative humidity (RH; Katsaros, 2001). Equation (1) can be rewritten in function of the components we are interested in disentangling (i.e., SST and RH):

$$Q_l = L_v C_e \rho_a W \left[q_s(SST) - RH \cdot q_s(SST + S)\right], \tag{2}$$

where $S = T_a - SST$ represents stability of the near-surface air. Assuming an analytical expression for the saturation specific humidity (Emanuel, 1994; Richter & Xie, 2008):

$$q_s(t) = q_0 \exp\left(\beta(t)\right), \tag{3}$$

$$\beta(t) = \exp\left(\gamma/x - c\ln(t)\right), \tag{4}$$

where β is a function of temperature (t), $\gamma = a - b$, and q_0, a, b, and c are constants.

The latent heat flux is then expressed as

$$Q_l = L_v C_e \rho_a W q_o \left[\exp(\beta(SST)) - RH \cdot \exp(\beta(SST + S))\right]. \tag{5}$$

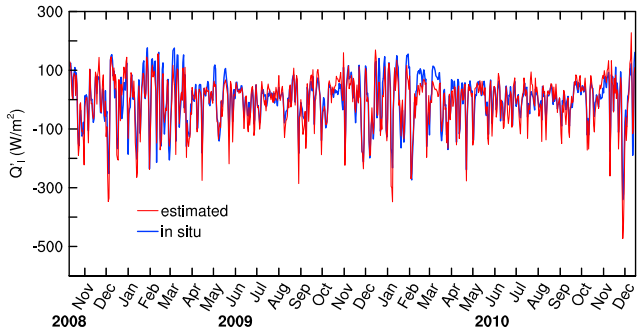

Figure 2. Observed latent heat flux anomalies (blue line; relative to 1-month running average) at the Woods Hole Oceanographic Institution/King Abdullah University of Science and Technology mooring (12 October 2008 to 16 December 2010) and the linearized latent heat flux anomalies estimated as in equation (6) (red line).

Equation (5) can be linearized through a first-order Taylor expansion around a mean state ($Q'_l = Q_l - \bar{Q}_l$) to express the latent heat flux anomalies as the sum of the contributions by variations in sea surface temperature, near-surface stability, relative humidity, wind speed, exchange coefficient, and air surface density:

$$Q'_l = \frac{\partial Q_l}{\partial SST} SST' + \frac{\partial Q_l}{\partial S} S' + \frac{\partial Q_l}{\partial RH} RH' + \frac{\partial Q_l}{\partial W} W' + \frac{\partial Q_l}{\partial C_e} C'_e + \frac{\partial Q_l}{\partial \rho_a} \rho_a'. \quad (6)$$

Each partial derivative in equation (6) is obtained analytically by differentiating equation (5) with respect to each of its variables as done by Richter and Xie (2008; see Appendix A). To evaluate the relative contribution of the zonal (u) and meridional (v) components of wind, we further decompose the wind speed term in equation (6) by expressing W in equation (5) as $W = \sqrt{u^2 + v^2}$ (Vimont et al., 2009).

In our decomposition, Q'_l refers to monthly mean anomaly perturbations. Figure 2 shows the time series of latent heat flux anomalies ($\tilde{Q}'_l$) estimated using equation (6) (and the terms in Appendix A) in relation to the Q'_l obtained directly as $Q'_l = Q_l - \bar{Q}_l$, where Q_l is the latent heat flux at day k and $\bar{Q}_l$ is the monthly average. The variability of latent heat flux perturbations estimated as the sum of the contributions of the different terms represents well the Q'_l, even though we assumed a simple analytical expression for the saturation specific humidity. The linear correlation coefficient between the two time series is 0.93, with a mean difference ($Q'_l - \tilde{Q}'_l$) of 7.9 W/m^2 and a *rmsd* of 32.9 W/m^2. If we consider only the winter period (October to March), the mean difference is larger (15.4 W/m^2), but the *rmsd* is lower (21.3 W/m^2), and the correlation coefficient is higher (0.95).

3.4. Westward Wind Events and Severe Sea Heat Losses

Bower and Farrar (2015) suggested that the SLP composite (and some daily fields) associated with the largest sea heat losses from Papadopoulos et al. (2013) seems connected with westward winds over the northern Red Sea. To investigate this conjecture, we reproduce the work of Papadopoulos et al. (2013) and compare the occurrence of westward wind/dry-air outbreak events with the severe heat loss days. However, instead of using OAFlux fields (Yu et al., 2008), as did Papadopoulos et al. (2013), we use heat fluxes from the MERRA-2 reanalysis, which are self-consistent with the wind fields we are analyzing and have higher spatial resolution than OAFlux.

Table 1
Evaluation of the Daily-Average MERRA-2 Winds and Evaporation Rates Against In Situ Observations at the Woods Hole Oceanographic Institution/King Abdullah University of Science and Technology Mooring (22.17°N; 38.5°E) for the period 12 October 2008 to 16 December 2010

	W (m/s)	u (m/s)	v (m/s)	E (m/year)
MERRA-2	3.86 [0.20, 10.14]	1.63 [−7.94, 5.38]	−2.53 [−8.63, 9.60]	1.64 [0.24, 5.00]
Mooring	4.85 [0.19, 11.81]	2.17 [−9.00, 7.34]	−3.36 [−9.21, 11.33]	2.00 [0.31, 7.10]
	σW (m/s)	σu (m/s)	σv (m/s)	E (m/year)
MERRA-2	2.10	1.75	2.69	0.89
Mooring	2.51	2.40	2.84	1.20
	$\mu(\Delta)$	*rmsd*	r	
ws	−0.99	1.13	0.89	
u	−0.54	1.11	0.90	
v	0.83	1.11	0.92	
E	−0.39	0.59	0.89	

Note. The upper block shows the mean [minimum, maximum] for wind speed (W), zonal velocity (u), meridional velocity (v), and evaporation rates (E) for each data set. The middle block shows the respective sample standard deviation (σ). The lower block shows the mean difference ($\mu(\Delta)$) between the second Modern-Era Retrospective analysis for Research and Applications (MERRA-2) and in situ observations, the root-mean-square of the difference (*rmsd*), and the linear correlation coefficients (r), which are significantly different from zero at 95% confidence.

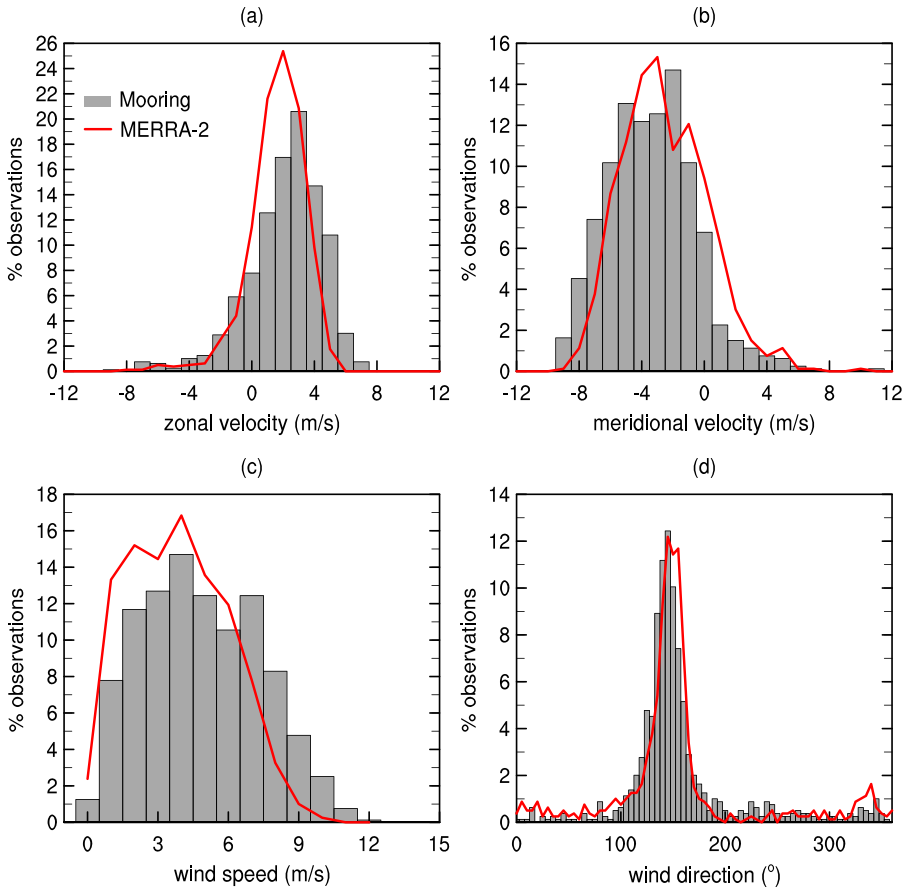

Figure 3. Histograms from daily-average in situ winds collected at the Woods Hole Oceanographic Institution/King Abdullah University of Science and Technology mooring (gray bars) and the MERRA-2 reanalysis (red curves) at the closest grid point (22.0°N–38.75°E) to the mooring position: (a) zonal velocity *u*; (b) meridional velocity *v*; (c) wind speed; and (d) wind direction. Histograms were computed using bins of 1 m/s for wind speed, *u*, *v* and 5° for wind direction. Vertical axes are the percentage of 796 daily data (12 October 2008 to 16 December 2010) that fall in the respective bins. Notice the different vertical axis scales used in the subplots. MERRA-2 = second Modern-Era Retrospective analysis for Research and Applications.

The 5% lowest daily turbulent heat flux (latent plus sensible heat flux) values define the severe heat loss days in Papadopoulos et al. (2013). They used only the turbulent terms instead of a complete heat balance because these terms have much higher variability than the radiative terms in the northern Red Sea as discussed in their section 3. The fifth percentile is determined from a composite time series of daily turbulent fluxes between December and February (DJF, hereafter). This time series is formed by averaging the turbulent heat flux values from the most northern part of the basin (25–28°N). For the OAFlux data used by Papadopoulos et al. (2013), the composite time series included 11 grid points, but for MERRA-2, it includes 24 grid points since MERRA-2 has higher horizontal grid resolution than the OAFlux. Papadopoulos et al. (2013) found no difference if their area was 23–28°N or 27–28°N.

4. Results

4.1. Evaluation of MERRA-2 Winds and Evaporation Rates

The comparison between MERRA-2 and in situ observations from the WHOI/KAUST mooring for the period between October 2008 and December 2010 indicates that MERRA-2 reproduces the basic characteristics of the wind regime and the evaporation at the mooring location (Table 1). The linear correlation coefficients are high, about 0.9, for all variables evaluated here (wind speed, zonal and meridional velocities, and evaporation), and *rmsd* is relatively low (1.1 m/s for winds and 0.59 m/year for evaporation). No apparent biases exist in MERRA-2, but the reanalysis tends to underestimate the wind strength as shown in Table 1 (upper

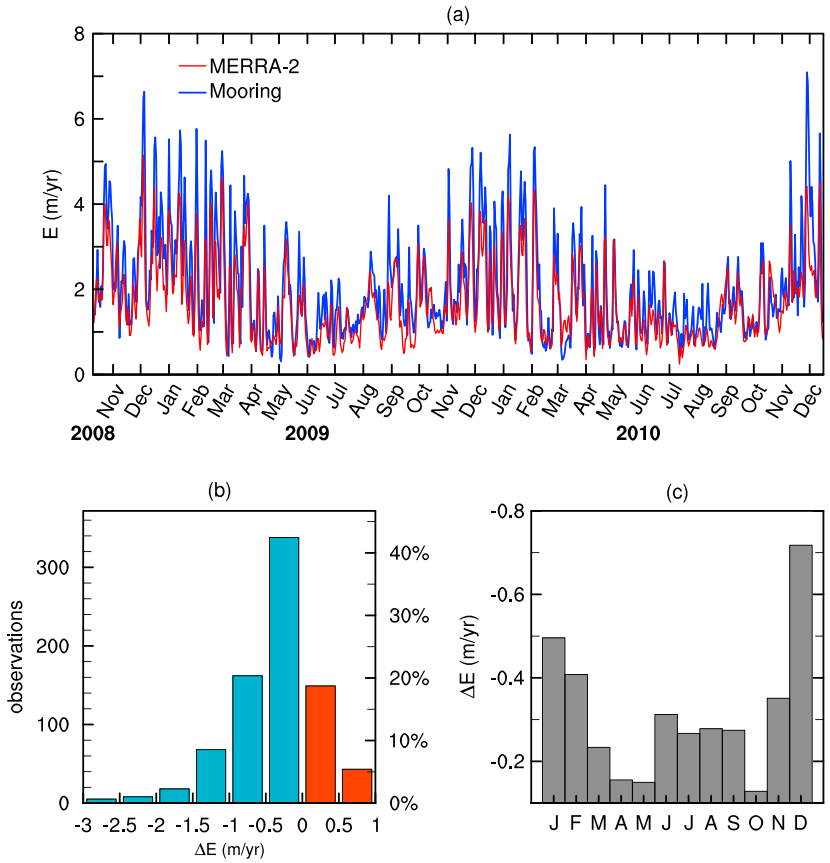

Figure 4. Comparison between daily-average evaporation rates calculated from in situ measurements at the Woods Hole Oceanographic Institution/King Abdullah University of Science and Technology mooring and the MERRA-2 reanalysis for the period between 12 October 2008 and 16 December 2010. (a) Time series of evaporation rates. (b) Histogram of the evaporation rate differences between the MERRA-2 and the Woods Hole Oceanographic Institution/King Abdullah University of Science and Technology mooring data (ΔE = MERRA-2 − Mooring). Blue/red are used to positive/negative differences. (c) Seasonal distribution of the mean differences in evaporation. MERRA-2 = second Modern-Era Retrospective analysis for Research and Applications.

block). Despite that, the statistical distribution of all wind variables of MERRA-2 is similar to the ones obtained from in situ observations (Figure 3), which provide an assurance that MERRA-2 reanalysis captures the essential features of the wind regime including the westward winds of interest here. Moreover, the correlation coefficient is also high between MERRA-2 and the land-based daily-average tower observations (0.78/0.76 [speed/zonal winds]), with *rmsd* of the same order as the mooring observations (1.19/1.17 m/s). With the 35-year-long time series of Wejh (26.199°N) and Yenbo (24.144°N), correlations for wind speed are 0.74 and 0.62, respectively, and *rmsd* is 1.26 and 1.23 m/s.

Water cycle variables such as evaporation typically present significant uncertainties in atmospheric reanalysis products (Bosilovich et al., 2017; Roberts et al., 2012; Yu et al., 2017). These uncertainties have several causes from model physics and parametrizations to the effects of an evolving observing system. In the northern Red Sea, the MERRA-2 reproduces well the variability of the evaporation at the WHOI/KAUST mooring location as can be seen in Figure 4a.

On the global scale, MERRA-2 has global mean evaporation larger than precipitation (Bosilovich et al., 2017; Yu et al., 2017). However, in the northern Red Sea, the reanalysis tends to underestimate the evaporation rates with a mean difference of −0.4 m/year (Figure 4b), which is consistent with the weaker winds over the Red Sea shown in the reanalysis. MERRA-2 also underestimates the mean, the standard deviation, and the maximum and minimum evaporation rates at the WHOI/KAUST mooring location (Table 1). Regarding the seasonal distribution, the most substantial underestimation occurs in winter (0.4–0.8 m/year), especially in December (Figure 4c), which is the period when the winds tend to be less stable (Menezes et al., 2018).

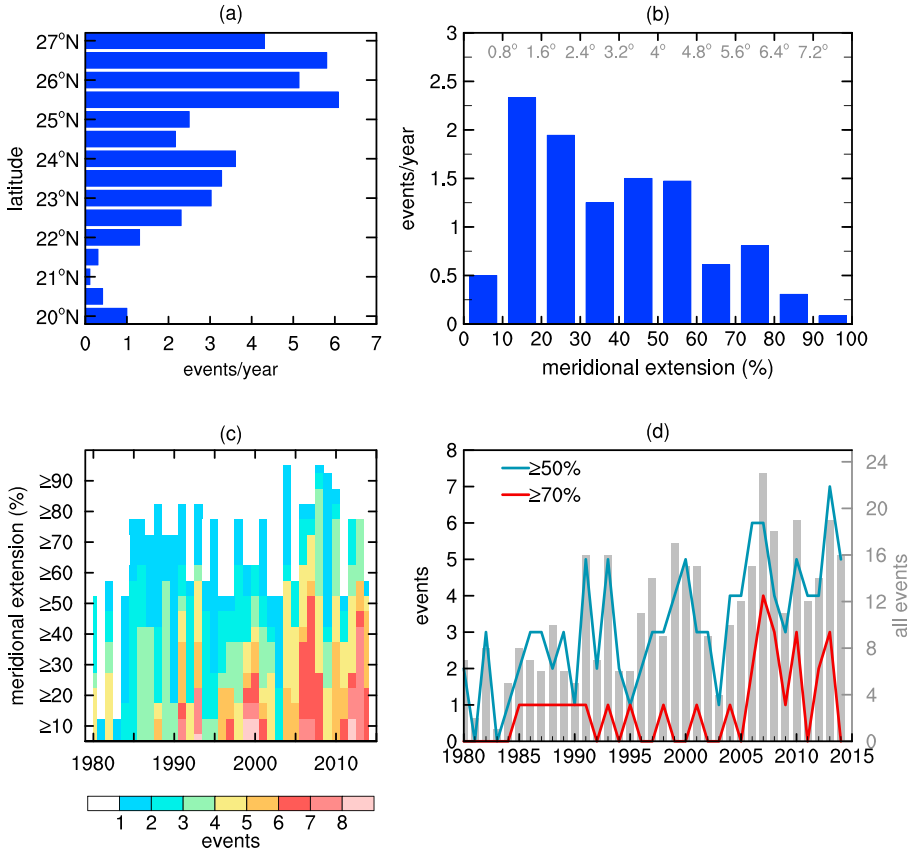

Figure 5. Statistics of the Red Sea westward wind events between 1980 and 2015 in winter in the second Modern-Era Retrospective analysis for Research and Applications: (a) frequency of events by latitude (total number of events at each latitude *j*/36 years); (b) histogram of the meridional extension of westward wind events. The histogram was computed using bins of 10%, which is equivalent to 0.8° of latitude. Bottom axis gives the percentage of the northern Red Sea meridional extension (20–28°N, which exclude the two gulfs in the extreme north). Top axis gives the meridional extension in degrees of latitude. (c) The number of events in winter between 1980 and 2015 in function of their meridional extension. For example, events in 2010 refer to the period October 2010 to March 2011. (d) The number of events in winter that extend to more than 50% (≥4°) and 70% (≥5.6°) of the northern Red Sea latitudes (curves) and the total number of events (gray bars). Blue/red curves use the left axis and gray bars on the right axis.

4.2. Westward Wind Events in MERRA-2

Similar to the QuikSCAT data analyzed by Menezes et al. (2018), MERRA-2 also shows two regions in the northern Red Sea with pronounced westward wind events: 23–24°N (three to four events per year) and 25.5–26.5°N (six events per year; Figure 5a). Different from QuikSCAT, there are fewer westward wind events south of 21°N, which suggest that the interpretation by Menezes et al. (2018) is correct, that is, most of the westward winds south of 21°N are associated with the RSCZ presence. Our statistics only include westward winds over the northern Red Sea that come from land. As in QuikSCAT, small-scale westward wind events are more common than large-scale events (≥50% of the northern Red Sea latitudes; Figure 5b).

From the 14 westward wind events detected at the WHOI/KAUST mooring by Menezes et al. (2018), nine events are winds from land according to MERRA-2. The events in MERRA-2 have similar duration as the in situ data (Table 2). Three events are associated with the RSCZ, and for one event, there are westward winds in MERRA-2, but they are not over the mooring position. In comparison with the in situ observations, MERRA-2 does not capture westward winds only for a single event (9 March 2010). In this case, MERRA-2 shows northward winds over the entire Red Sea. Nevertheless, MERRA-2 is a good indicator of the occurrence and timing of the westward wind events.

Besides the year-to-year changes in the frequency of westward wind events, already reported by Menezes et al. (2018), MERRA-2 shows decadal modulations (e.g., between 1995 and 2005) and a long-term positive trend in the occurrence of westward wind events (Figures 5c and 5d). The total number of events, which

Table 2
Westward Wind Events Recorded at the Woods Hole Oceanographic Institution/King Abdullah University of Science and Technology Mooring and MERRA-2 Between October 2008 and December 2010

	Mooring		MERRA-2	
	Start	Duration (days)	From land	Characteristic
01	2008-12-03	5	Yes	Duration = 6 days
02	2008-12-17	6	Yes	Duration = 6 days
03	2009-01-14	4	Yes	Duration = 4 days
04	2009-10-23	4		RSCZ
05	2009-12-02	2		RSCZ
06	2009-12-24	2	Yes	Duration = 2 days
07	2010-01-02	2	Yes	Duration = 1 day
08	2010-01-07	11	Yes	Duration = 8 days
09	2010-01-29	5		RSCZ
10	2010-03-09	8		Northward winds over the entire Red Sea
11	2010-04-03	3		Westward winds are found northward of the mooring, at 24°N
12	2010-10-19	3	Yes	Duration = 3 days
13	2010-11-11	3	Yes	Duration = 2 days
14	2010-11-23	14	Yes	Duration = 12 days

Note. Westward winds at the mooring are from Menezes et al. (2018, their Table 2). The first column is the event number (temporal order). The second and third columns show the start date and the event duration as recorded at the Woods Hole Oceanographic Institution/King Abdullah University of Science and Technology mooring, respectively. The fourth column indicates if the westward winds are from land as determined from the second Modern-Era Retrospective analysis for Research and Applications (MERRA-2). The fifth column shows the duration of the westward events in MERRA-2 and indicates if the westward winds are associated with the Red Sea Convergence Zone (RSCZ) or with other wind patterns.

includes narrow and large-scale ones, grow from less than eight events per winter in the 1980s to more than 16 in recent years (Figure 5d, gray bars). Not only did the overall number of events increased but also the occurrence of large-scale events. For example, events broader than 4° of latitude (≥50% of the northern Red Sea meridional extension) doubled from 1–3 per winter (1980–1990) to 3–7 events (2005–2015; Figure 5d, blue curve). Until 2005, events covering almost the entire northern Red Sea (≥70%; ≥5.6° of latitude) were unusual, but in the last decade, these events become more prominent with four events in 2007 and three events in 2010 and 2013 (Figure 5d, red curve).

4.3. Large-Scale SLP Pattern During Westward Wind Events

This section describes the large-scale atmospheric circulation pattern through SLP that favors the surface winds to blow westward over the northern Red Sea in winter. We are particularly interested in westward wind events that cover a large meridional extension of the northern Red Sea (≥50%) as their frequency is increasing over time (see the previous section), and they can strongly impact the evaporation; the primary driver of the basin-scale Red Sea overturning circulation.

Figure 6a shows the SLP and wind composites for the 79 westward wind events between 1980 and 2015 with meridional extension greater than 4° of latitude (large-scale westward wind events). Most of these events occurred in January (31.6%) and December (30.4%). Events in November accounted for 15.2%, February for 6.3%, and October for only 1.3% of the large-scale events. As a reference, Figure 6b shows similar composites for winter (same period) but excluding all the westward wind events that are wider than 1.6° of latitude (20% of the northern Red Sea). Thus, the winter composites reflect the conditions associated with the typical Red Sea along-axis wind regime.

In the winter monsoon, three semipermanent pressure systems control the Middle East climate and weather (Vojtesak et al., 1991; Vorhees, 2006; Walters & Sjoberg, 1988):

a. the Siberian High (also known as the Siberian Anticyclone, Asiatic High, or Central Asia High);

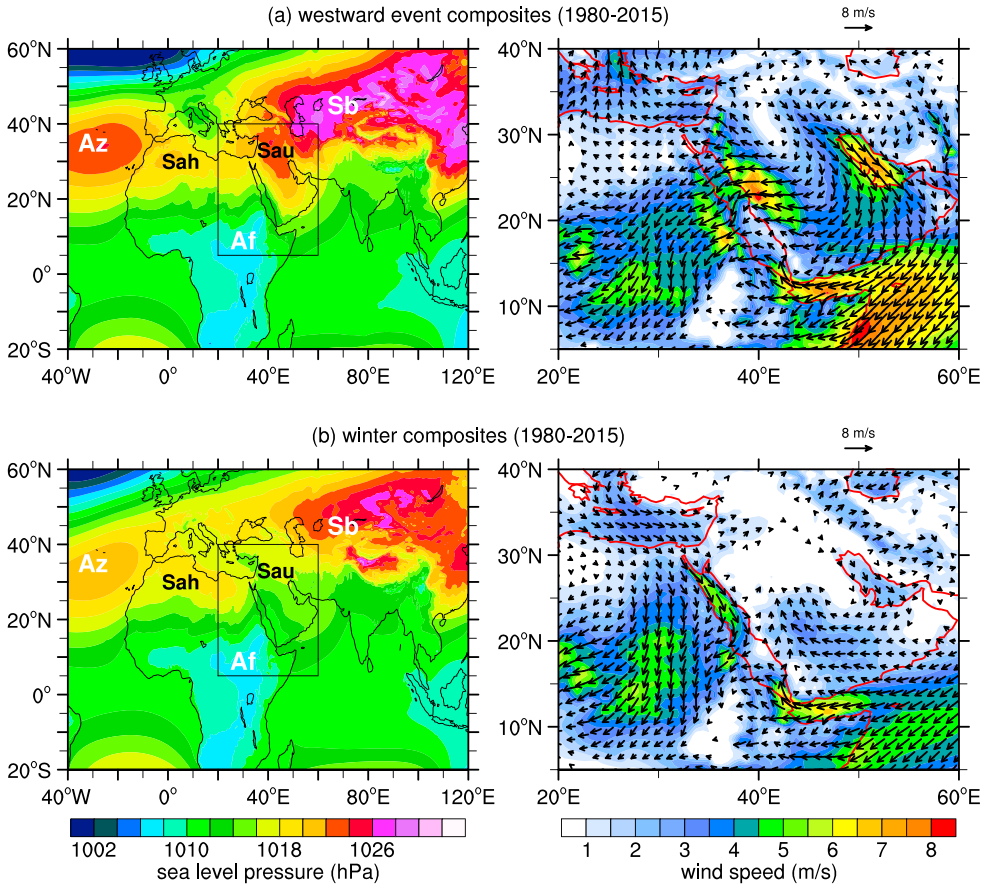

Figure 6. The second Modern-Era Retrospective analysis for Research and Applications sea level pressure (left) and surface wind (right) composites for (a) 79 westward wind events between 1980 and 2015 that extend for more than 4° of latitude in the northern Red Sea. (b) Winter, same period. The winter composites exclude all fields that have westward wind events extending for more than 1.6° of latitude (20% of the northern Red Sea meridional extension). In 35 years, there are 5,760 winter days with no westward wind event ≥1.6° (87.8%). Right panels are a detailed view of the winds in the box shown in the sea level pressure maps. Only vectors stronger than 0.5 m/s are plotted. Az stands for the Azores High, Sah for the Saharan High (the eastward extension of the Azores High), Sau for the Saudi Arabian High, Sb for the Siberian High, and Af for the African/Sudanese Low.

b. the Azores High (also known as the North Atlantic/Subtropical High/Anticyclone, or Bermuda-Azores High) and its eastward extension (the Saharan High); and
c. the African/Sudanese Low.

Besides the above large-scale semipermanent features, the subsynoptic-scale Saudi Arabian High (or Arabian High) is also an essential player in the Middle East in the winter monsoon (Hasanean et al., 2013; Vojtesak et al., 1991; Vorhees, 2006; Walters & Sjoberg, 1988). Radiative cooling over the desert initiates and maintains this pressure feature (Vojtesak et al., 1991). The Saudi Arabian High tends to disappear during frontal passages, reforming after them. Another synoptic atmospheric feature at lower tropospheric levels that affect the weather in the Middle East is the RST (e.g., Awad & Almazroui, 2016; de Vries et al., 2016, 2013; Krichak et al., 1997a, 1997b; Krichak et al., 2012; Tsvieli & Zangvil, 2005; 2007, and references therein). The RST is a temporary extension of the African/Sudanese Low, characterized by a low-pressure tongue extending northward over the Red Sea toward the Eastern Mediterranean and its surroundings. Typically, the RST develops in autumn but can also occur in spring and winter (Awad & Almazroui, 2016; de Vries et al., 2016, 2013). The RST systems are classified as nonactive, associated with hot and dry weather conditions, and active, associated with heavy precipitation and flash flooding in the Middle East (e.g., de Vries et al., 2013; Krichak et al., 2012; Shentsis et al., 2012; Tsvieli & Zangvil, 2005, 2007). The active RST (ARST) is linked to an intensified Arabian Anticyclone in the southeastern margin of the Arabian Peninsula, which

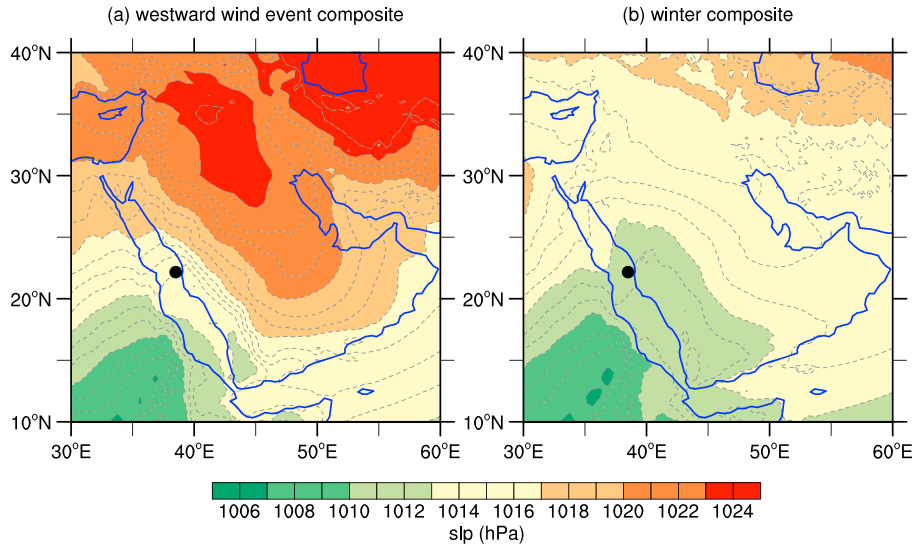

Figure 7. Zoom over the Arabian Peninsula of the second Modern-Era Retrospective analysis for Research and Applications sea level pressure (SLP) composite maps for (a) 79 westward wind events between 1980 and 2015 that extend for more than 4° of latitude in the northern Red Sea. (b) Winter, same period. Dashed gray contours are SLP every 1 hPa. Black dot shows the Woods Hole Oceanographic Institution/King Abdullah University of Science and Technology mooring position.

enhances moisture transport from the Arabian Sea and the Gulf of Aden toward the Red Sea (e.g., Dasari et al., 2018; de Vries et al., 2016, 2018).

Three significant differences in the SLP pattern exist when the winds are predominantly westward over the northern Red Sea in relation to the winter composite (Figure 6). First, the semipermanent Azores High centered at about 30°W–35°N is intensified (1,022–1,026 hPa). Second, the Siberian High is stronger (≥1,026 hPa) and extends much more westward (until about 40°E). Together with the Azores High, it forms a band of relatively high pressures between 30°N and 50°N from the Atlantic to the Pacific Ocean. Third, during the westward wind events, there is an elongated feature with relatively high SLP (1,020–1,026 hPa) over the Arabian Peninsula that seems to be part of the Siberian High. Because the SLP over northeast Africa is relatively low (1,008–1,014 hPa) south of 30°N—both Saharan High and Sudanese Low have much lower SLP than the Arabian High—there are substantial pressure gradients over the Red Sea, especially in the northern part (Figure 7a). In the northern Red Sea, the isobars are straight across the central Red Sea axis, indicating that geostrophic winds flow from the Arabian Peninsula to Africa (Figures 6a, right, and 7a).

In the winter composite (which excludes desert-origin westward winds), the SLP over the Arabian Peninsula is lower (1,010–1,018 hPa)—the Sudanese Low prolongs over the Peninsula—and the pressure gradients over the Red Sea are weaker than in the westward wind event composite (Figures 6 and 7b). Moreover, the Saharan High (the Azores High eastward extension) has higher pressures than the Saudi Arabian High, which is much weaker and located in the southeast of the Peninsula when compared with the westward wind event composite (Figures 6, right). In the winter composite, the winds have the expected along-axis pattern: southward in the northern Red Sea, northward in the southern Red Sea, and the RSCZ in the middle at about 18–19°N (Figure 6b, right).

In westward wind events, the core of the Saudi Arabian High (maximum SLP) is, on average, located at the northern part of the Arabian Peninsula (around 33–35°N), lying between the Eastern Mediterranean and the Zagros Mountains and extending southward along the central axis of the Peninsula (Figure 7a). This high-pressure tongue projects to the Arabian Desert, with pressure steadily decreasing. In westward wind events, the isobars over the northern Red Sea do not have a pronounced inverted V shape that characterizes the ARST (e.g., de Vries et al., 2013; Krichak et al., 1997b). We will return to the differences between the westward wind/dry-air outbreak events and the ARST in section 4.7.

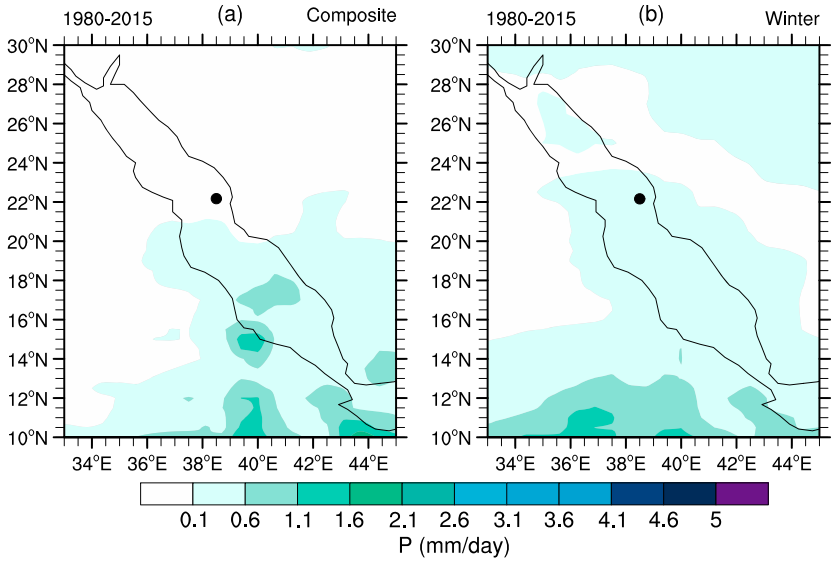

Figure 8. The second Modern-Era Retrospective analysis for Research and Applications precipitation composites for (a) 79 westward wind events between 1980 and 2015 that extend for more than 4° of latitude in the northern Red Sea; (b) winter, same period. The winter composites exclude all fields that have westward wind events extending for more than 1.6° of latitude (20% of the northern Red Sea meridional extension). Black dot shows the Woods Hole Oceanographic Institution/King Abdullah University of Science and Technology mooring position.

4.3.1. Precipitation and Surface Air Temperature During Westward Wind Events

Rainfall in westward wind events is negligible. Figure 8 shows the precipitation composite for the 79 westward events between 1980 and 2015 and the winter composite excluding all westward wind events. The mean precipitation in MERRA-2 is below 0.1 mm/day in the northern Red Sea during the events, which is lower than the winter mean rainfall in the region. Precipitation over land and ocean is also small for each event individually (Figure S3). In agreement with MERRA-2, the rain gauge at the WHOI/KAUST mooring also did not record heavy precipitation coincident with westward wind events (Table 3). For the nine westward wind events coming from land recorded at the mooring, the maximum daily accumulated precipitation was only 0.29 mm (11 November 2010), and in four events, there was no rain at all.

Besides precipitation being low, the Arabian Peninsula is cooler during westward wind events (Figure 9)—another characteristic that contrasts with both ARST and nonactive RST systems (e.g., Krichak et al., 2012; Tsvieli & Zangvil, 2005, 2007). In westward wind events, most of the Peninsula has air surface temperatures around 8–12 °C (greenish in Figure 9), with temperatures also lower over the Sahara Desert and the Siberian High area (see also Figure S4 showing a close look over the Arabian Peninsula). The incursion of colder winds over the Arabian Peninsula seems to originate in the Zagros, Elburz, and Caucasus Mountains, between the Black and the Caspian Seas (Figure 10a), which is consistent with a more northward location of the Arabian High. Near the Red Sea, the westward wind event composite resembles the air surface temperature map from Jiang et al. (2009) for the event on 14 January 2009, although in their snapshot, as expected, the surface temperatures are much lower (below 6 °C). According to Jiang et al. (2009), adiabatic compression causes the Arabian Desert-originated cold air to heat as it flows downhill from the central plateau to the Red Sea coastal plain. Figure 10a pattern agrees with this description, with the streamlines transitioning from greenish (colder) to reddish (warmer) in the coastal plain.

In contrast with the westward wind events, the temperatures in the winter composite vary from 15 °C in the northern part up to 28 °C in the southern part of the Peninsula. In the southern region, the warm winds are coming from the Arabian Sea and the Persian Gulf (Figure 10b). Not surprisingly, the winter air surface temperature fields used to form the composite present higher standard deviations (Figure S5).

4.3.2. Westward Wind and Winter Shamal Events

During westward wind events, the enhanced Arabian High extending along the central axis of the Arabian Peninsula causes an anticyclonic (clockwise) circulation over most of the Peninsula with intensified and colder southward winds (8 m/s) over the Persian Gulf (Figures 6a and 10a). These winds are a signature of

Table 3
Westward Wind Events at the Woods Hole Oceanographic Institution/King Abdullah University of Science and Technology Mooring: Maximum Daily-Average Evaporation (E), Wind Speed (W), Relative Humidity (RH), Zonal Velocity (u), Air-Sea Temperature Difference ($S = T_a - SST$), Air Surface Temperature at 10 m (T_a), Air-Sea Saturation Specific Humidity Difference ($\Delta q = q_s - q_a$), Precipitation (P), the Day When the Maximum Evaporation Occurred, and the Event Number

E (m/year)	W (m/s)	RH (%)	u (m/s)	S (°C)	T_a (°C)	Δq (g/kg)	P (mm)	Day (max)	Event
7.09	9.27	31.78	−9.00	0.94	29.51	15.62	0.24 (0.06)	2010-11-29	14
6.64	8.60	32.99	−6.97	−1.01	27.16	15.88	0.00 (0.00)	2008-12-06	01
5.73	10.00	43.71	−7.03	−1.48	24.69	12.22	0.00 (0.00)	2009-01-14	03
5.63	8.49	39.91	−7.46	0.13	27.02	12.64	0.13 (0.10)	2010-01-09	08
5.57	7.35	40.43	−4.10	−1.67	26.49	14.55	0.00 (0.00)	2008-12-18	02
5.01	5.53	42.51	−4.19	0.45	31.62	15.42	0.29 (0.07)	2010-11-11	13
3.56	5.29	50.64	−1.07	−2.45	25.47	12.67	0.00 (0.00)	2009-12-24	06
3.52	5.16	45.16	−3.25	−0.11	27.29	12.04	0.03 (0.03)	2010-01-02	07
2.28	2.27	60.03	−1.77	0.95	32.09	9.91	0.12 (0.06)	2010-10-20	12
1.52	1.64	61.98	−1.63	−0.87	29.73	10.69	0.00 (0.00)	2009-10-24	04*
1.38	1.71	74.82	−0.48	−1.96	27.12	7.86	16.96 (13.49)	2009-12-03	05*
0.95	2.93	72.82	−2.93	1.20	28.14	4.37	0.00 (0.00)	2010-04-04	11*
0.92	4.67	75.85	−1.91	0.55	27.42	4.35	0.16 (0.07)	2010-03-14	10*
0.83	2.61	72.69	−2.15	−0.17	26.56	5.69	0.00 (0.00)	2010-01-30	09*
r_{max}	0.91	−0.97	−0.86	−0.12[a]	−0.09[a]	0.90			
r_{event}	0.73	−0.80	−0.76	0.13[a]	−0.01[a]	0.75			
r_{winter}	0.84	−0.75	0.58	−0.65	−0.43	0.73			

Note. All data are from the day of maximum evaporation. P shows the total precipitation (accumulated rain) from the hourly time series. Values between parentheses are the maximum precipitation over 1 hr. Events marked with asterisk (*) are not from the Arabian Desert according to the second Modern-Era Retrospective analysis for Research and Applications (see Table 2) and indeed have weak evaporation ($E \leq 1.5$ m/year). Lower block shows the linear correlation coefficients (r) between evaporation and the other variables. r_{max} refers to the maximum evaporation rates, r_{event} for all observations during desert-origin westward wind events, and r_{winter} for winter excluding these events. The correlations are significantly different from zero at 95% of confidence, except the coefficients marked with superscripted "a" ([a]).

Shamal ("north" in Arabic) events. Winter Shamal winds are strong southward winds (≥8.5 m/s) over the Gulf that occur once or twice a year, notably from December to February, and are associated with adverse weather conditions such as dust storms (Al Senafi & Anis, 2015; Perrone, 1979; Rao et al., 2001; Shi et al., 2004). These Shamal events can have a duration of 24–36 hr or last for 3–5 days (Perrone, 1979). The Shamal events bring cold, dry air over the Gulf, leading to excessive evaporation and severe heat loss from the sea (about 1,000 W/m^2) that may trigger the formation of the salty Persian Gulf Water (Swift & Bower, 2003;

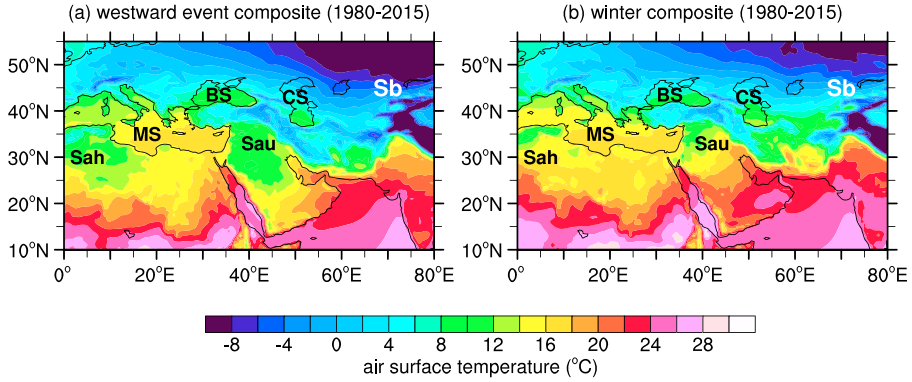

Figure 9. The second Modern-Era Retrospective analysis for Research and Applications air surface temperature composites for (a) 79 westward wind events between 1980 and 2015 that extend for more than 4° of latitude in the northern Red Sea; (b) winter, same period. The winter composite excludes all fields that have westward wind events extending for more than 1.6° of latitude. Sah stands for the Saharan High, MS for the Mediterranean Sea, BS for the Black Sea, CS for the Caspian Sea, Sau for the Saudi Arabian High, and Sb for the Siberian High (see Figure 6 for the pressure systems).

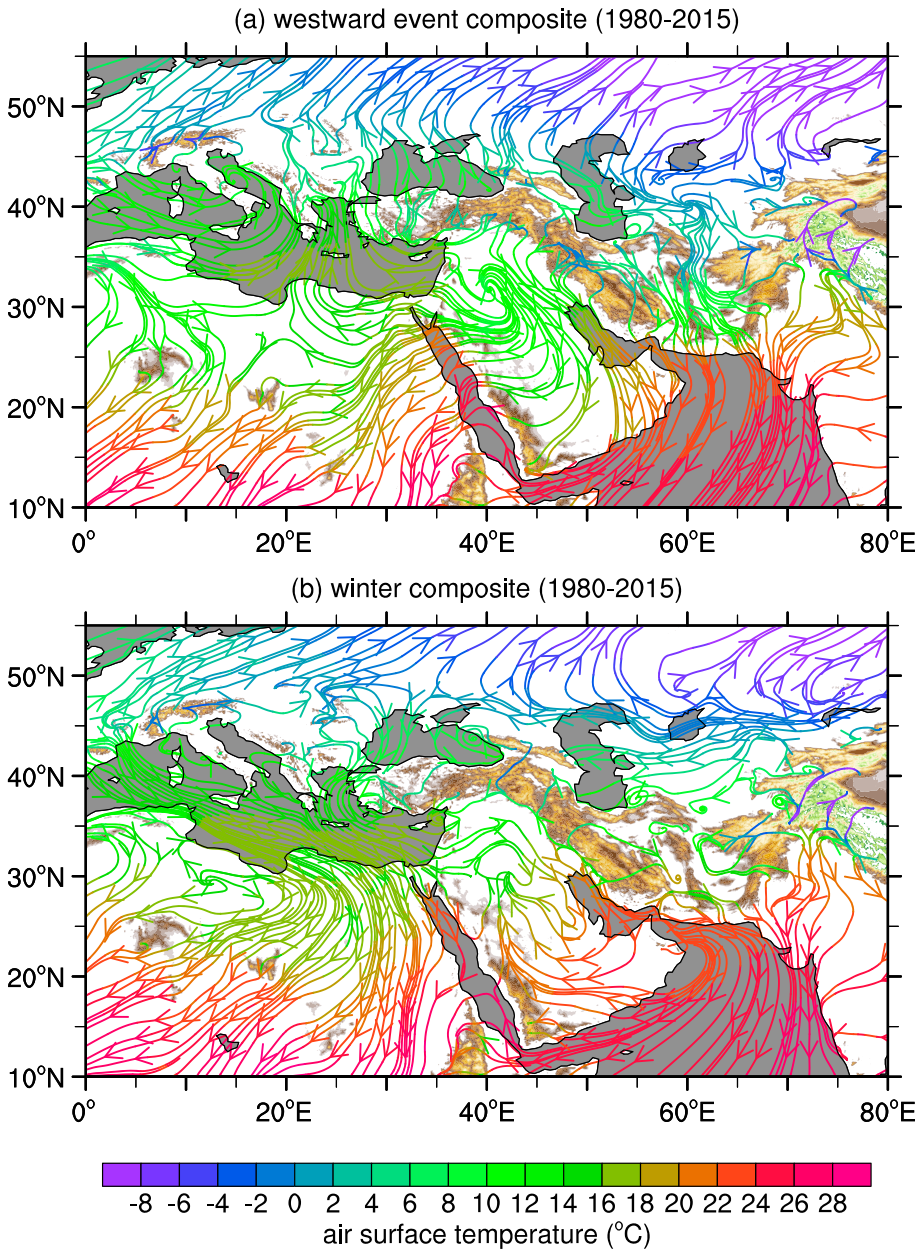

Figure 10. The second Modern-Era Retrospective analysis for Research and Applications wind composite streamline maps colored by their surface temperatures: (a) large-scale westward event composite (1980–2015); (b) winter, same period. The winter composite excludes all fields that have westward wind events extending for more than 1.6° of latitude. Brown/green shadings are land elevations above 1,000 m from ETOPO2 data set. Seas/oceans are depicted in gray.

Thoppil & Hogan, 2010). Pressure gradients between the Arabian High and lower pressures in the Gulf of Oman sustain the winter Shamal winds (Perrone, 1979; Rao et al., 2001). Hence, the westward wind composite suggests that the winter Shamal winds in the Persian Gulf and the westward wind events over the northern Red Sea may be part of the same feature (the enhanced Arabian anticyclonic circulation).

Compared with the winter composite, the winds are stronger in the Gulf of Aden and the northwest Arabian Sea during the westward wind events, but no notable differences in direction and strength are observed in the southern Red Sea between these two wind regimes (Figure 6). In the westward event composite, the winds flow from Saudi Arabia to Egypt in the northern Red Sea. Reaching Egypt, part of the flow heads southward and part northward into the eastern Mediterranean Sea. In the westward wind composite, there is no flow

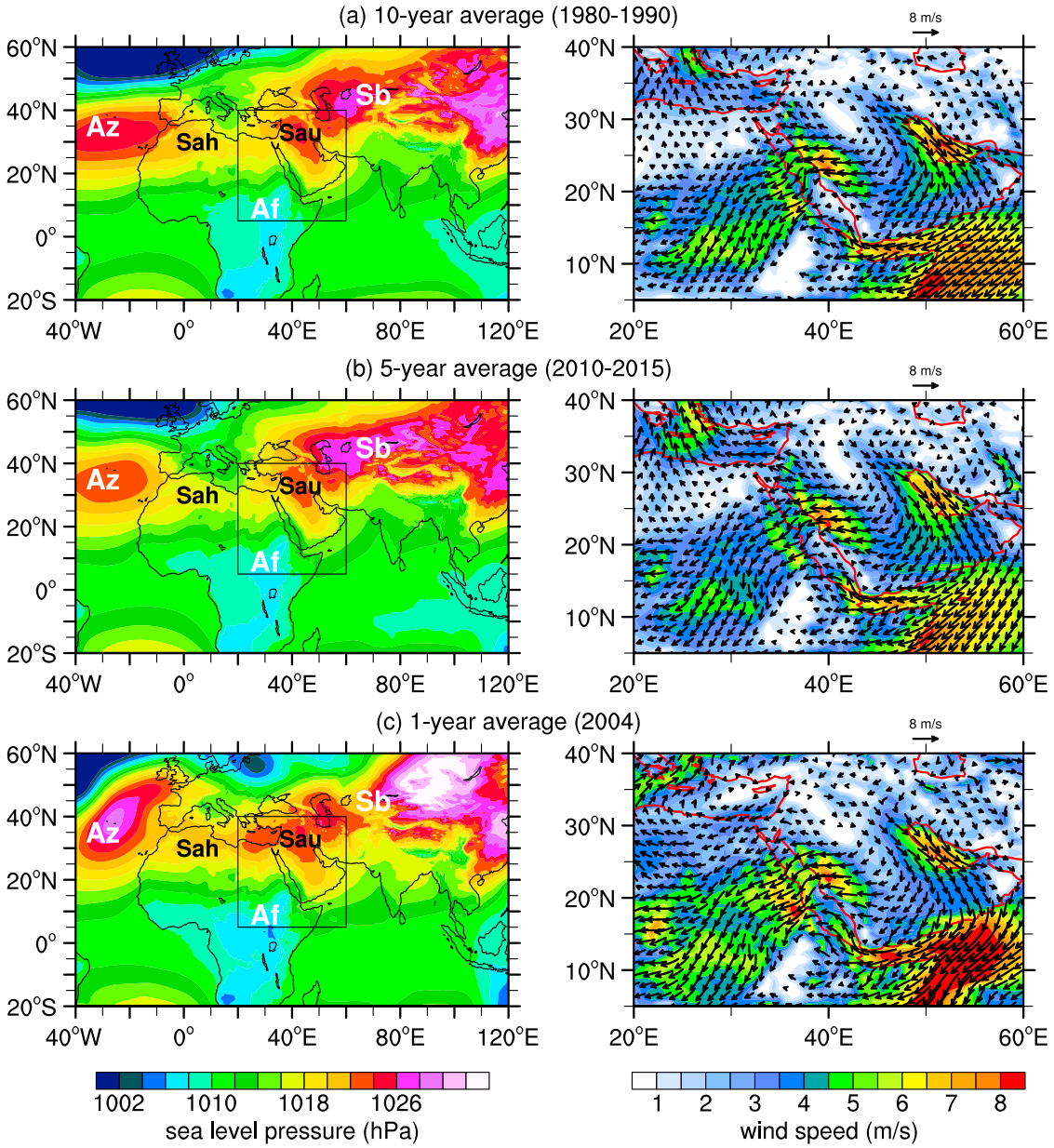

Figure 11. The second Modern-Era Retrospective analysis for Research and Applications sea level pressure (SLP; left) and surface wind (right) composites for westward wind events occurring between (a) 1980 and 1990 (13 events), (b) 2010 and 2015 (21 events), and (c) 2004 (3 events). The events used to construct the composites extend for more than 4° of latitude in the northern Red Sea. Right panels are a detailed view of the winds in the box shown in the SLP maps. Only vectors stronger than 0.5 m/s are plotted. Az stands for the Azores High, Sah for the Saharan High (the eastward extension of the Azores High), Sau for the Saudi Arabian High, Sb for the Siberian High, and Af for the African/Sudanese Low.

from the Mediterranean into the northern Red Sea. Contrarily, in the winter composite, the northern Red Sea winds originate in the Mediterranean Sea (Figure 10b).

We obtain similar patterns as described above (high SLP over the Arabian Peninsula, a stronger and more westward Siberian High, and an intensified Azores High) if the westward wind composites are calculated over different periods and averaging a different number of large-scale events (Figure 11). In all cases, concomitant with westward winds in the northern Red Sea, there is intensified southward winds over the Persian Gulf. Stronger winds also blow over the Gulf of Aden and the western Arabian Sea. The overall pattern is robust. It appears even if we average just a few events such as in Figure 11c, where the composite refers to three events in 2004 (one in February and two in December). In the region including the Red Sea,

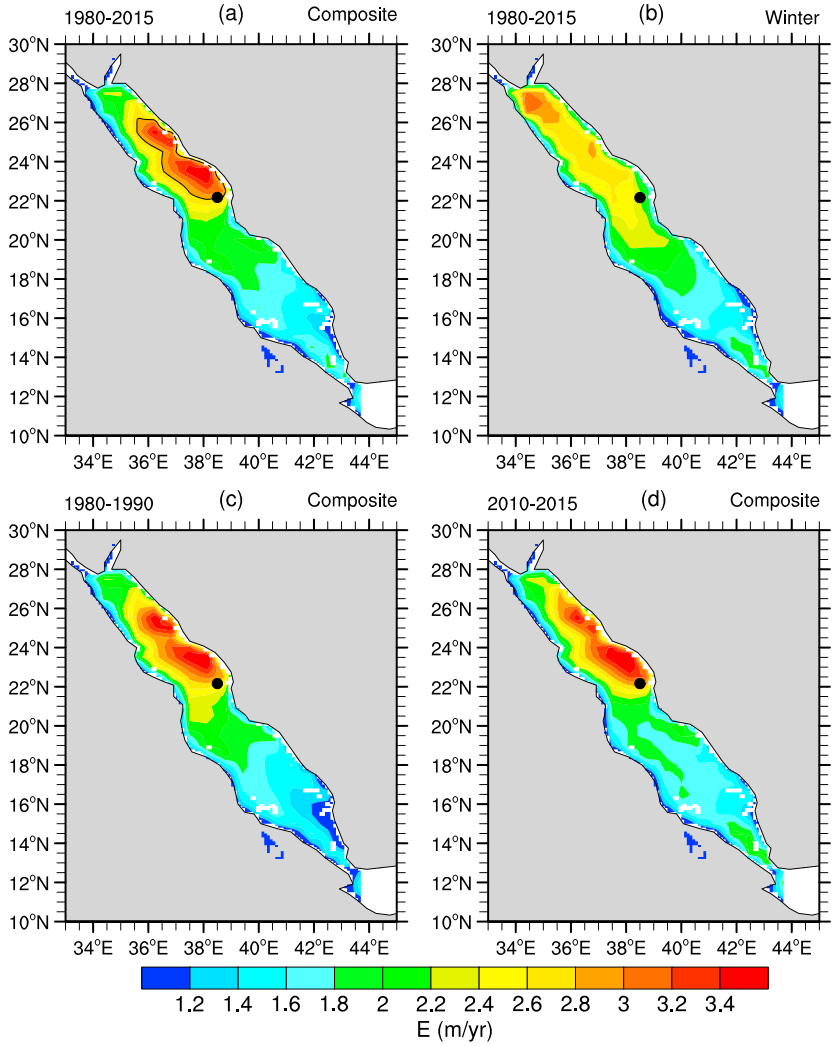

Figure 12. The second Modern-Era Retrospective analysis for Research and Applications evaporation rate composites for (a) 79 westward wind events between 1980 and 2015 that extend for more than 4° of latitude in the northern Red Sea; (b) winter, same period. The winter composites exclude all fields that have westward wind events extending for more than 1.6° of latitude; (c) for 21 westward wind events between 1980 and 1990 and (d) for 13 events between 2010 and 2015. Black dot shows the Woods Hole Oceanographic Institution/King Abdullah University of Science and Technology mooring position and the black contour in (a) is the 2.8-m/year isoline that encloses the area which will be later used as an index.

the Persian Gulf, and the Arabian Peninsula, the standard deviations of the SLP fields used to form the composites are relatively low (about 3–5 hPa) for both composites though slightly lower for the westward wind event (Figure S6).

4.4. Effects of Dry-Air Outbreaks on the Red Sea Evaporation

Figure 12 shows three composites for evaporation rates associated with large-scale westward wind events (dry-air outbreaks) and a winter composite, which was calculated excluding all westward wind events that are broader than 1.6° of latitude. Because the winter composite excludes most westward wind events, it represents the mean evaporation pattern associated with the typical winter along-axis wind regime.

The westward wind evaporation composites are for different periods (1980–2015, 1980–1990, and 2010–2015) and are averaged over a different number of events (13 to 79). Despite these differences, they have a very similar pattern. The highest evaporation rates (≥3.2 m/year) are on the eastern side of the northern basin between 22°N and 26°N, forming a pool that stands out in all maps. The WHOI/KAUST mooring is located on the southern flank of this high evaporation pool (Figure 12). During winter, this region is

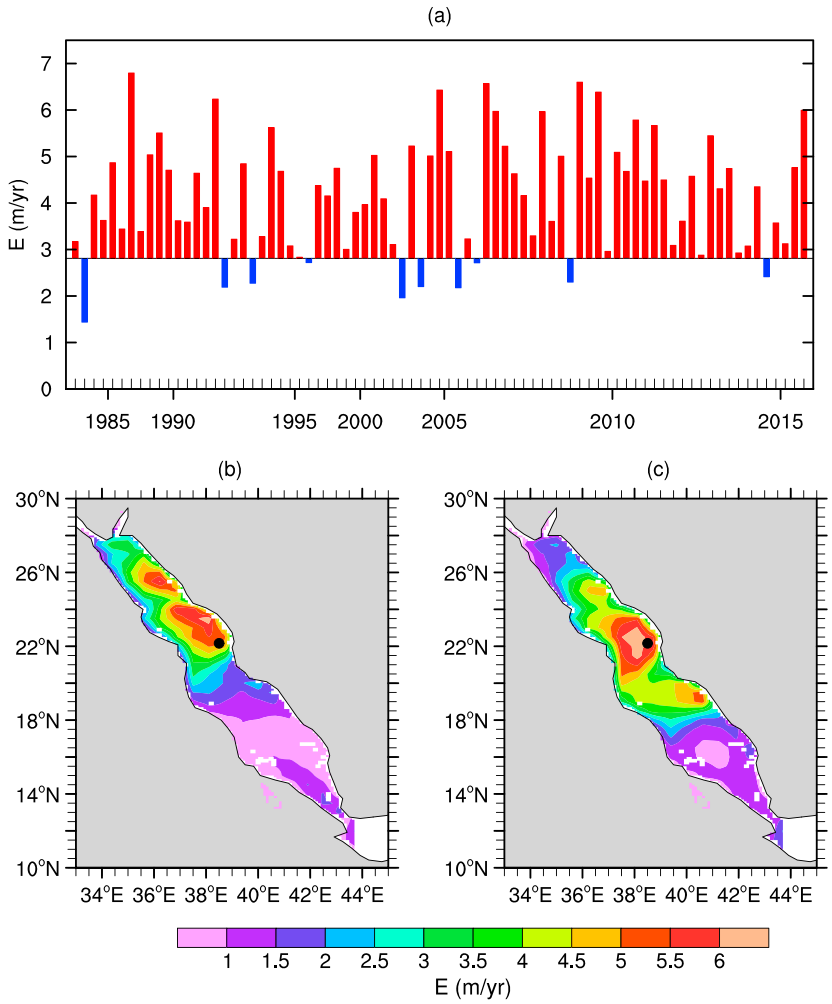

Figure 13. (a) Maximum evaporation rates in the area defined by the 2.8-m/year contour of the composite (Figure 12a) for the 79 large-scale westward wind events between 1980 and 2015. The horizontal axis is irregular in time (each tick mark corresponds to one event). Black line is the time average of the maximum evaporation rate in the same area in winter, excluding all westward wind events that extend for more than 1.6° of latitude. Red/blue bars are used for events with evaporation above/below the mean winter evaporation in the second Modern-Era Retrospective analysis for Research and Applications (2.81 m/year). (b) Evaporation rates on 14 January 2009 and (c) 27 December 2004. Black dots in (b) and (c) show the Woods Hole Oceanographic Institution/King Abdullah University of Science and Technology mooring position.

dominated by the northward-flowing surface Eastern Boundary Current (EBC) that is believed to be an essential piece of the Red Sea overturning circulation (Bower & Farrar, 2015; Sofianos & Johns, 2003; Zarokanellos, Papadopoulos, et al., 2017).

Model simulations (e.g., Eshel & Naik, 1997; Sofianos & Johns, 2003; Yao, Hoteit, Pratt, Bower, Kohl, et al., 2014; Yao, Hoteit, Pratt, Bower, Zhai, et al., 2014) and some observations (Bower & Farrar, 2015; Zarokanellos, Papadopoulos, et al., 2017) indicate that the surface EBC carries warm and relatively low-salinity surface waters, becoming cooler, more saline, and denser as it progresses northward due to intense air-sea fluxes. The composites suggest that the high evaporation associated with the large-scale westward winds may induce surface water mass transformation in the surface EBC. Notice the surface EBC seems to be different from the northward-flowing subsurface current (around 80 m) that carries the Gulf of Aden Intermediate Water along the eastern boundary in summer and spring (e.g., Churchill et al., 2014; Wafar et al., 2016; Yao, Hoteit, Pratt, Bower, Zhai, et al., 2014; Zarokanellos, Kurten, et al., 2017). The subsurface EBC begins in the Strait of Bab al Mandab and reaches up to 22–24°N, while the surface EBC originates in the central Red Sea around 20°N as a crossover of a western boundary current and extends to the extreme

north (Bower & Farrar, 2015; Sofianos & Johns, 2003; Yao, Hoteit, Pratt, Bower, Kohl, et al., 2014; Zhai, Pratt, & Bower, 2015). However, determining whether these currents have different dynamics is outside the scope of the present paper.

The spatial pattern associated with the westward winds is very distinct from the typical winter condition where the evaporation rates steadily increase northward, with the maximum in the extreme north between 26°N and 28°N (3–3.2 m/year; Figure 12b).

The composites described above reflect the general spatial pattern during the westward wind/dry-air outbreak events. However, there are substantial differences between events in quantities such as wind speed, air temperature, and humidity and, therefore, in evaporation rates (latent heat flux). To illustrate the temporal variability in evaporation rates associated with the events, we construct an event evaporation index that is defined as the maximum evaporation rates in the area defined by the 2.8-m/year contour of the composite in Figure 12a. For each event, the evaporation index in Figure 13a is from the day when the westward winds have the maximum meridional extension. As a reference, the solid line shows the time average of the winter index (2.81 m/year). The winter-index time series is defined in the same way as the event evaporation index but excluding all days with westward wind events broader than 1.6° of latitude. In most events, the evaporation in the eastern boundary is larger than the mean winter-index evaporation (red bars in Figure 13a). There are events strongly evaporative with rates above 6 m/year in MERRA-2, but most events have rates between 3 and 5 m/year. Although the evaporation associated with dry-air outbreaks has growth and decay phases in interannual and decadal time scales, no long-term trend is apparent.

Despite the temporal variability in the evaporation rates, the spatial patterns in snapshots resemble the composite fields with the highest evaporation on the eastern side of the Red Sea. For instance, Figures 13b and 13c show two snapshots of the evaporation field associated with the events of 14–15 January 2009 and 27–28 December 2004 (same dates from Figure 1). In both cases, the maximum evaporation pool (≥6 m/year) locates around 22–23°N. During these strongly evaporative dry-air outbreak events, most areas of the northern Red Sea experience rates greater than 3.5 m/year. The 14–15 January 2009 event is of interest because there are concurrent in situ measurements at the WHOI/KAUST mooring, and several works have previously studied it (e.g., Bower & Farrar, 2015; Jiang et al., 2009; Kalenderski et al., 2013; Menezes et al., 2018). For this event, the WHOI/KAUST mooring recorded maximum daily-average evaporation of 5.7 m/year.

The westward winds bring arid conditions offshore, and this is one of the reasons why we refer to them as dry-air outbreaks (Figure 14). Typically, the mean relative humidity from October to February (excluding all westward wind event days) is around 60% (dashed lines in Figure 14). However, during westward wind events, daily-average relative humidity sharply drop during westward wind events as much as 30%, such as in the long-standing event of November–December 2010 (14-day duration). This event has the highest daily-average evaporation rate (about 7 m/year) of the 2-year-long in situ record at the WHOI/KAUST mooring.

Table 3 describes for all events detected at the mooring, the maximum evaporation and associated wind speed, relative humidity, precipitation, zonal velocity, air-sea temperature difference ($S = T_a - SST$), air surface temperature, and air-sea humidity difference ($\Delta q = q_s - q_a$). According to MERRA-2, five of these events did not originate at the Arabian Desert (see Table 2). The evaporation and relative humidity of four of these events corroborate the MERRA-2 findings. In these four events, the evaporation is below 1.5 m/year, the relative humidity is above 70%, and Δq is lesser than 8 g/kg, which suggests that the winds are not from the Arabian Desert. For most of the desert-origin events (according to MERRA-2), the maximum daily in situ evaporation is above 5 m/year, relative humidity is below 50%, and Δq is above 12 g/kg (Table 3).

For the event of November/December 2010, the maximum evaporation in MERRA-2, at the closest grid point to the mooring, is 4.5 m/year, but it reaches 6.9 m/year at 23.5°N, which is of the same order as the in situ data. If we exclude all westward wind events, the mean in situ evaporation in winter is 2.29 m/year, and maximum evaporation reaches 5.76 m/year. Therefore, eight westward wind events cause evaporation more substantial than the winter mean and in two events the evaporation rates are above 6 m/year (Table 3). These two extreme evaporative events have the highest air-sea humidity differences (≥15 g/kg), which are higher than the maximum associated with other wind regimes in winter (14.56 g/kg).

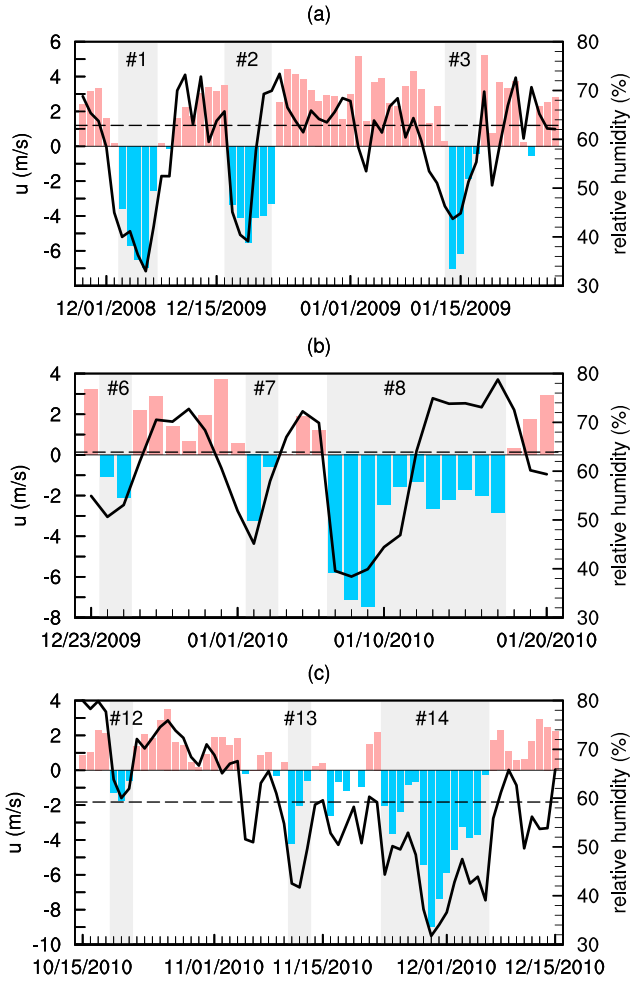

Figure 14. Daily-average zonal velocities (u) and relative humidity measured at the Woods Hole Oceanographic Institution/King Abdullah University of Science and Technology mooring for nine westward wind events. Each panel contains three westward wind events (blue bars/gray shadings). Relative humidities are the black curves (right axis), and bars are zonal velocities (left axis). Pink/blue bars are used for positive/negative values (eastward/westward winds). Top labels are the event number from Table 2. Dashed black lines indicate the mean relative humidity in the period, excluding westward wind events dates. In (a), the mean relative humidity is 62.8%, in (b) is 63.9% and in (c) 59.2%.

4.5. Latent Heat Flux Decomposition: Understanding What Controls the Intense Evaporation in Dry-Air Outbreaks

Although the events with strong westward winds tend to have significant evaporation rates (Table 3), the relationship, as expected, is not linear because evaporation depends on other variables such as air surface temperature and relative humidity (see, e.g., equation (2)). For example, the event starting on 3 December 2008 (event 01) has a maximum wind speed of 8.6 m/s and evaporation of about 6.6 m/year, while the event starting on 17 December 2008 (event 03) is stronger but is less evaporative. To disentangle the contribution of the various parameters affecting the latent heat fluxes (evaporation) during westward wind events, we decompose the latent heat flux perturbations as the sum of contributions by variations in surface relative humidity, near-surface stability, SST, wind speed, exchange coefficient, and air density using equation (6).

Figure 15a shows the estimated net (accumulated) latent heat flux perturbations due to variations in SST, near-surface stability (air-sea temperature difference), relative humidity, and wind speed, the most important terms in our decomposition. Here the perturbations are relative to monthly mean latent heat fluxes that are always negative (heat loss by the sea) and have values between −274 to −124 W/m^2 in winter. In westward wind events, the most critical factors contributing to the high evaporation are the relative humidity and the wind speed. In several events, relative humidity contributes more to the net latent heat loss than the wind strength (e.g., events 01, 03, 08, 12, and 13). For the most evaporative event of November 2010 (event

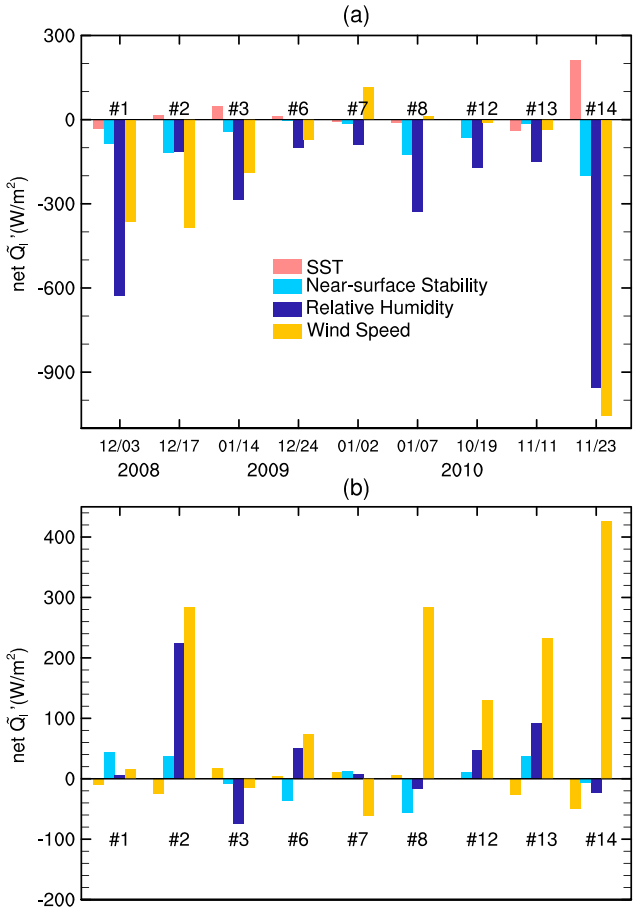

Figure 15. Net contribution to latent heat flux perturbations by variations in sea surface temperature (SST), near-surface stability, relative humidity, and wind speed estimated using equation (6) and the Woods Hole Oceanographic Institution/King Abdullah University of Science and Technology observations. (a) For the nine westward wind events shown in Figure 14. For each event, the net $\tilde{Q}_l'$ is the cumulative sum for the in situ event duration of Table 2, starting in the beginning of the event (bottom axis). (b) For the same duration but prior to the westward wind events. In this case, the $\tilde{Q}_l'$ is integrated backward (reverse cumulative sum) starting the day before the onset of the respective westward wind event. Labels # are the event number from Table 2.

14) with evaporation around 7 m/year and relative humidity of 30%, the contributions of wind speed and relative humidity are of the same order. In winter, apart from westward wind events, the wind strength is the latent heat flux's major contributor (Figure 15b). The critical role of relative humidity in removing heat from the sea during westward wind events is even more evident when we look at the evolution of the latent heat flux perturbations (Figure 16). Although the time series of the heat flux perturbations (red curve) has a similar shape as the wind speed contribution (yellow curve), about half of the magnitude of the negative peaks is due to the relative humidity contribution (cf. the vertical axes for the three time series). In westward wind events, most of the wind strength contribution to the latent heat loss is due to variations in the zonal component (Figure 17).

The lower block of Table 3 shows the linear correlation coefficients between evaporation and the other variables. During westward wind events, evaporation is more strongly (inverse) correlated with the relative humidity than the wind speeds, confirming the result of the decomposition analysis above. Correlations are also high with air-sea specific humidity difference and zonal velocity, but evaporation is not significantly correlated with the air surface temperature (T_a) and near-surface stability (S). Whether we compute correlations for winter but excluding the desert-origin westward wind events, the correlation with S and T_a are statistically significant (Table 3, last row). In this case, wind speeds can explain most of the evaporation rates in winter, followed by relative humidity and near-surface stability.

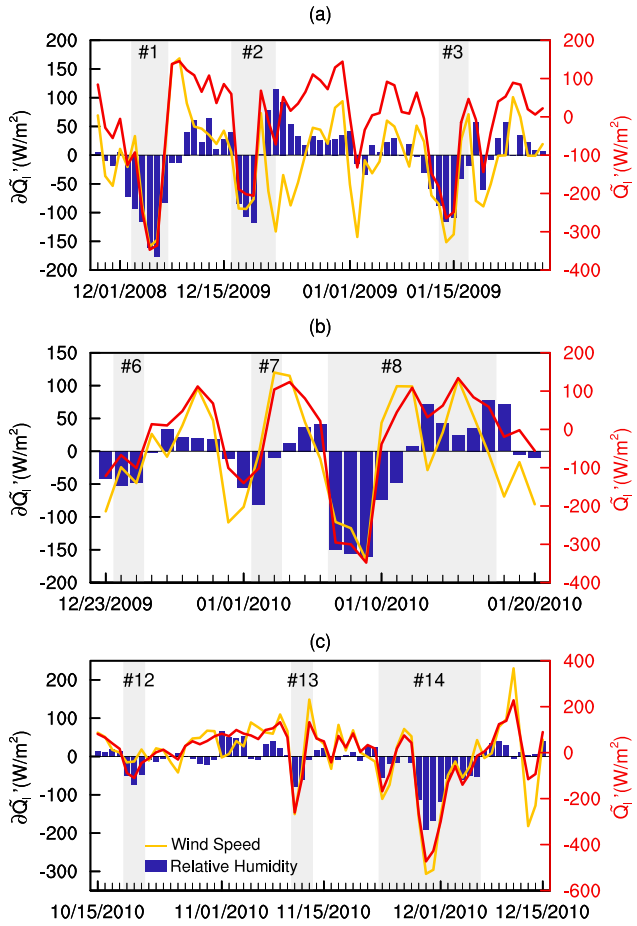

Figure 16. Contribution to latent heat flux perturbations by variations in relative humidity (bars) and wind speed (yellow curve) estimated ($\partial\tilde{Q}_l'$) using equation (6) and the Woods Hole Oceanographic Institution/King Abdullah University of Science and Technology observations for the nine westward wind events shown in Figure 14. Red curve (using the right axis) is the sum($\tilde{Q}_l'$) of all contribution terms in equation (6). Each panel (a–c) contains three westward wind events highlighted by the gray shadings. Top labels are the event number from Table 2.

In summary, major evaporative westward wind events in the northern Red Sea arise from relatively strong zonal winds carrying dry air, with both wind speeds and relative humidity being significant factors controlling the latent heat loss during the events. In the westward wind events, thermal parameters (SST, air surface temperature, and near-surface stability) are not relevant, and this is another reason why refer to the westward wind events as dry-air outbreaks.

4.6. Westward Wind Events and Severe Sea Heat Losses in the Northern Red Sea

As shown in the previous sections, the westward wind/dry-air outbreak events sharply increase the evaporation, that is, latent heat flux at the surface, in the eastern boundary of the northern Red Sea due to intensified dry winds. Papadopoulos et al. (2013) studied the severe heat losses from the sea north of 25°N between December and February. Some of their 5% extreme negative values indicate westward winds in the northern Red Sea (see, e.g., their Figures 8 and 9). Thus, it is pertinent to ask how many days of severe sea heat loss are concurrent to the westward wind events?

To answer the above question, we matched up the strongest heat loss days (fifth percentile) and the westward wind event dates. We also examined whether the extreme values (first percentile) are connected with the occurrence of westward wind events. Since the westward winds affect the eastern side of the basin more than its most northern part (Figure 12), we also matched the occurrence of westward winds to the strongest heat loss days in the eastern boundary. In the latter case, a time series composite was formed by averaging the turbulent heat flux values from 17 grid points in the area defined by the 2.8-m/year contour of the

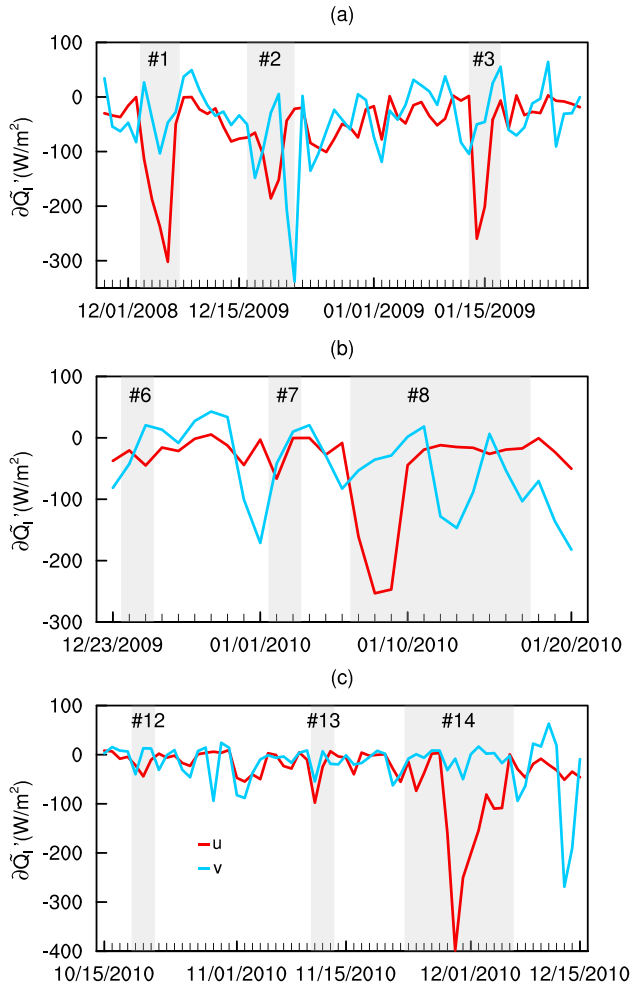

Figure 17. Contribution to latent heat flux perturbations by variations in the zonal (u) and meridional (v) wind components for the nine westward wind events shown in Figure 16. Each panel (a–c) contains three westward wind events highlighted by the gray shadings. Top labels are the event number from Table 2.

evaporation composite. Values of mean turbulent heat flux in DJF, first and fifth percentiles in these areas are given in Table 4.

The two areas (north of 25°N and the eastern boundary) have similar turbulent heat flux statistical distributions in MERRA-2 between December and February (Figures 18a and 18b), with the mean heat loss being slightly lower in the eastern basin. The fifth percentile in MERRA-2 for the area north of 25°N is somewhat smaller than the one calculated by Papadopoulos et al. (2013; 380 W/m^2).

Table 4
Turbulent Heat Flux Statistics: Mean, First, and Fifth Percentiles for Different Areas of the Northern Red Sea (See Text for Details)

Areas	Mean	5% (W/m^2) [days]	1% (W/m^2) [days]
Extreme North	−237.92	−391.28 [162]	−478.28 [32]
Eastern Margin	−243.98	−416.25 [162]	−496.53 [32]
Mooring	−237.58	−454.85 [10]	−510.82 [2]

Note. Mooring refers to the Woods Hole Oceanographic Institution/King Abdullah University of Science and Technology mooring data. [days] gives the number of days that turbulent heat loss is higher than the first and fifth percentiles.

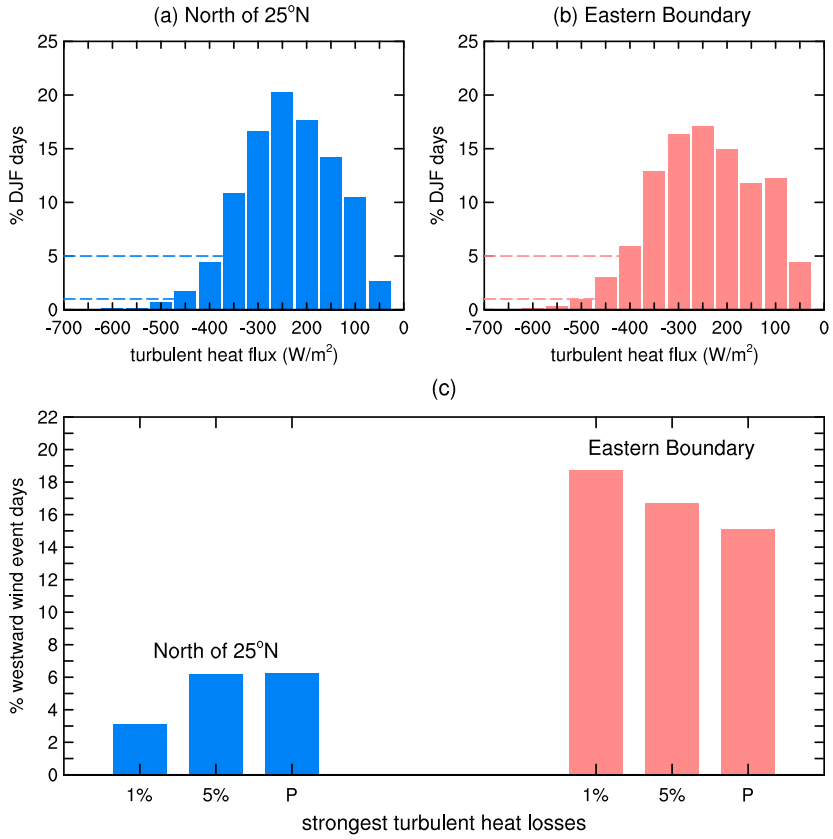

Figure 18. The second Modern-Era Retrospective analysis for Research and Applications histogram of turbulent heat flux in December-January-February (DJF) for the region between 25° N and 28° N (a) and in the eastern boundary (b). Dashed lines define the first and the fifth percentiles. (c) Concomitant westward wind events and severe heat loss days in the region between 25°N and 28°N and in the eastern boundary area for the first and fifth percentile and also for the value *P* correspondent to the fifth percentile of Papadopoulos et al. (2013; −380 W/m^2). Blue/pink bars are used for the northern/eastern boundary regions.

Comparing the largest heat loss days and the westward wind event dates, we found the westward wind events occurring at about 6% of those days in the northern region (Figure 18c, blue bars). No statistical difference exists if the fifth percentile value of Papadopoulos et al. (2013) is used (*P* in the same figure). For the most extreme heat losses, only 3% of the days correspond to the westward wind events in MERRA-2.

A different picture emerges in the eastern boundary region where westward wind events were concurrent with about 17% of the lowest turbulent heat losses (20% if we consider the first percentile; Figure 18c, pink bars). For the in situ observations (the mooring is located near the eastern boundary), the 10% lowest daily turbulent heat losses in DJF correspond to 20 days, with 50% of them being concurrent with westward wind events. For the fifth percentile, westward wind events account for 40% of these days. The two most extreme sea heat loss days in DJF at the mooring data correspond to westward wind events.

4.7. Differences Between Dry-Air Outbreaks and ARST Systems

The position of the intensified Arabian High is crucial to understand some characteristics of the large-scale westward wind/dry-air outbreak events, which are distinct from the ones associated with the ARST systems. None of 12 ARST systems identified by de Vries et al. (2013) correspond to westward wind events over the northern Red Sea in MERRA-2. In large-scale westward wind events, the intensified Arabian High is an elongated feature of the Siberian High. Its core, positioned in the central axis of the Arabian Peninsula, advects dry and relatively cold air from the Arabian Desert as we previously described, resulting in massive evaporation rates over the northern Red Sea. In the ARST case, the Arabian Anticyclone is located at the southeastern corner of the Peninsula, extending over the Persian Gulf, the Arabian Sea, and the Gulf of Aden. It advects warm and moister air toward the Red Sea following the RST, typically causing heavy rainfall

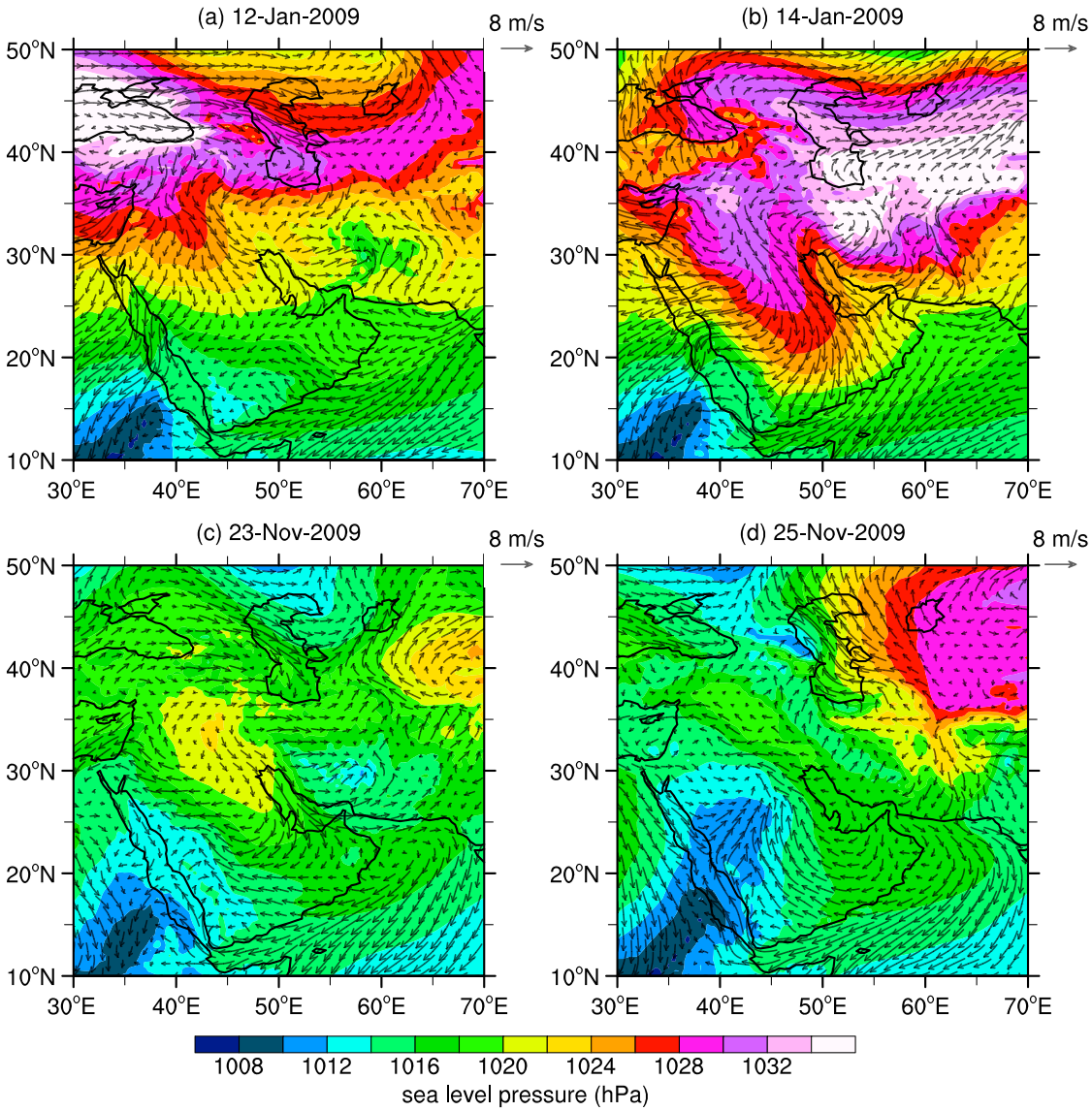

Figure 19. Large-scale westward wind event in the northern Red Sea in January 2009 (a, b) and the Active Red Sea Trough (ARST) event in November 2009 (c, d) in the second Modern-Era Retrospective analysis for Research and Applications. Colors are daily-average sea level pressure, and the overlaid vectors represent the daily-average surface winds. (a and c) Maps before the respective events. (b and d) Maps during the event. During the ARST (d), the Sudanese Low is prominent; it extends from Africa, passing over the Red Sea, and projecting into the Arabian Peninsula. Notice the anticyclonic circulation in the southeastern side of the Peninsula, which advect warm and moist air from the Arabian Sea and the Gulf of Aden. Before the ARST event, the SLP map in (c) shows an Arabian High eastward, but it is not sufficient to create the pressure gradients favoring the surface winds to blow westward over the northern Red Sea. Before the ARST, the winds over the Red Sea have the typical along-axis pattern for the winter monsoon. In the large-scale westward wind events (b), the Siberian High is much more intensified and westward than before the ARST event (c).

over the western Arabian Peninsula (e.g., near Jeddah) and the Eastern Mediterranean regions (depending on the upper troposphere pattern). See, for instance, Figure 1 of de Vries et al. (2016), and Figures 15 of de Vries et al. (2013) and Dasari et al. (2018).

To illustrate the differences between the large-scale westward wind events and the ARST systems and to demonstrate that these wind events are not ARST precursors, Figure 19 shows daily-average SLP and surface wind fields before and during

- a typical large-scale westward wind event (14–15 January 2009); and
- a typical ARST system (25 November 2009)

We chose the two examples above because they are well described in the literature (e.g., de Vries et al., 2013; Jiang et al., 2009; Kalenderski et al., 2013; Menezes et al., 2018). The ARST on 25 November 2009 caused extreme flooding in Jeddah, resulting in more than 100 fatalities and strongly impacting Saudi Arabia (de Vries et al., 2013). Notice that in November 2009, there is no westward wind event over the northern Red Sea recorded at MERRA-2, WHOI/KAUST in situ observations or the QuikSCAT/ASCAT scatterometer data (not shown).

Besides the westward wind event of 14–15 January 2009 (Figure 19b), we show in Figure S7 a large-scale westward wind event that occurred in November/December 2010 (maximum evaporation rate recorded on 29 November 2010). The aim is to exemplify that the fundamental differences between the ARST and the large-scale westward wind event SLP patterns in Figure 19 are not due to the seasonal cycle; large-scale westward wind events over the northern Red Sea always have characteristics different from ARST events.

In the ARST event of 25 November 2009, the Sudanese Low is prominent; it extends from Africa, through the Red Sea, and projects into the Arabian Peninsula (Figure 19d). The SLP and surface wind patterns in Figure 19d resemble the geopotential height and wind fields at 1,000 hPa from de Vries et al. (2013) for the same date (25 November 2009; their Figure 10d). It is also similar to the 1,000-hPa geopotential height map in the RST event of 15 October 1987 (de Vries et al., 2013, their Figure 5d). This ARST Sudanese Low pattern is absent in the large-scale westward wind events of 14–15 January 2009 (Figures 19a and 19b) and November 2010 (Figure S7).

In large-scale westward wind events, the Sudanese Low does not project into the Arabian Peninsula (see, e.g., Figures 19a, 19b, S6, and the composite map in Figure 7), and the Siberian High is much more westward than in the ARST. In the westward wind events, the Arabian High elongates from the Siberian High as a high-pressure tongue along the central axis of the Arabian Peninsula. This feature sets large pressure gradients that favor the winds flow from Saudi Arabia to Egypt. During the ARST system, this high-pressure tongue feature is not observed (Figure 19d).

Before the ARST onset (23 November 2009), there is a relatively high-pressure system over the Arabian Peninsula (Figure 19c), but it is not an extension of the Siberian High, and its position is much eastward. As a consequence, this system does not create the pressure gradients that favor westward winds over the northern Red Sea. The surface winds on 23 November 2009 have the typical along-axis pattern: toward the south in the northern Red Sea and toward the north in the southern Red Sea, with a convergence zone around 19–20°N. We again restate that in November 2009, no large-scale westward wind event over the northern Red Sea was recorded.

Overall, the Arabian Peninsula is cold at the surface during the 14–15 January 2009 westward wind event, with a low-temperature feature over the Peninsula resembling the high-pressure sea level tongue of the Arabian High (Figure S8). When we look around the end of the westward wind event of 14–15 January 2009, the Sudanese Low is not projected into the Arabian Peninsula such as it is at the end of the ARST (Figure S9). To conclude, Figure S10 shows the evaporation rates caused by the westward wind event of 14–15 January 2009 and the ARST event of 25 November 2009. As can be seen, the ARST is not associated with extreme evaporation over the northern Red Sea. Therefore, the characteristics of westward wind events over the northern Red Sea and ARST systems (including the onset and the ending) are distinct.

5. Summary & Discussion

The present study examined the MERRA-2 reanalysis and a unique 2-year record of in situ observations from an offshore mooring deployed by WHOI/KAUST in the northern Red Sea. Our study aimed to determine the large-scale atmospheric conditions that favor the surface winds to flow westward over the northern Red Sea in winter and the effects of these transient but common events on the evaporation rates of the Red Sea. In analogy to the cold-air outbreaks, we refer to the westward wind events as dry-air outbreaks.

The SLP composite analysis showed that the onset of the westward wind events over the northern Red Sea connects with large-scale synoptic processes in midpolar and subpolar latitudes. During the westward wind events, the semipermanent Siberian High is enhanced and extends much more westward than in typical winter conditions. A characteristic feature in the westward wind event composites is the elongation of the Siberian High over the Arabian Peninsula, forming a tongue-like feature of high SLP. This feature indicates an intensification of the Arabian High, an essential feature controlling the climate and weather of the Middle

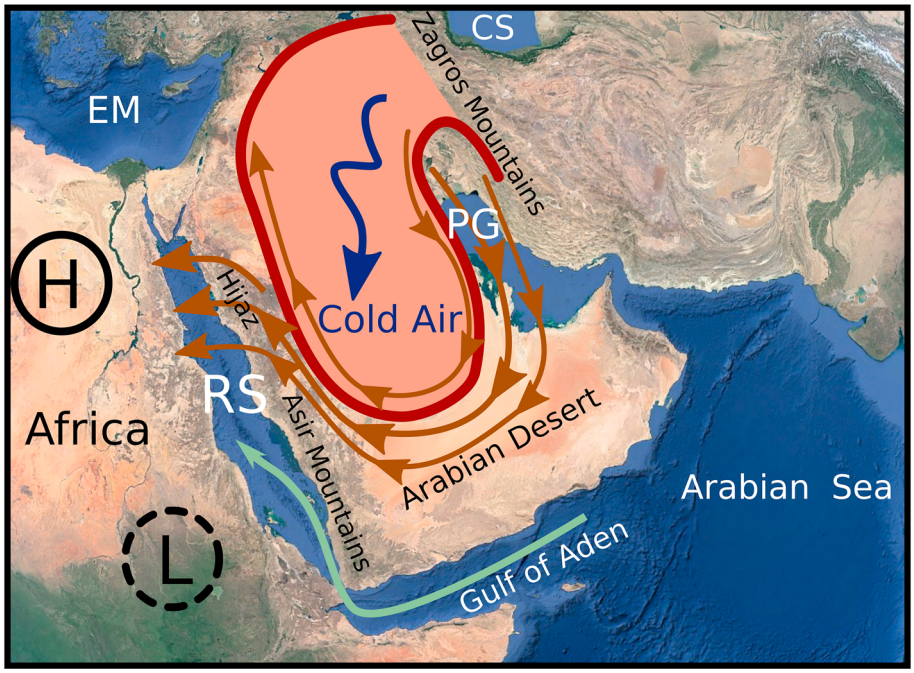

Figure 20. Schematic representation of the westward wind/dry-air outbreaks over the northern Red Sea in winter. H indicates for the Saharan High and L the Sudanese Low over the African continent. The reddish feature over the Arabian Peninsula represents the enhanced Arabian High that seems to be a prolongation of the Siberian High (not shown in this schematic). When the Arabian High is prominent at the north of the Peninsula and the sea level pressures over Africa are lower, the large-scale pressure gradients favor the winds from Saudi Arabia to Egypt. The Arabian High, at its northern position, brings extratropical, cold surface air over the Peninsula. The cold air seems to originate at the Caucasus, Taurus, and the Zagros Mountains, similar to the winter Shamal winds over the Persian Gulf (Perrone, 1979; Walters & Sjoberg, 1988). As depicted in the schematic, the surface wind circulation over the Peninsula is anticyclonic (arrows indicate the wind direction). Blowing from the Arabian Desert the westward winds are dry. During the dry-air outbreaks, the northern Red Sea loses a substantial amount of heat (latent) to the atmosphere through evaporation, and the eastern margin feels most the effects. RS stands for the Red Sea, EM to the Mediterranean Sea, CS to the Caspian Sea, and PG to the Persian Gulf. Brownish curves are used to represent dry winds and greenish for moist winds.

East in winter (Hasanean et al., 2013; Vojtesak et al., 1991; Vorhees, 2006; Walters & Sjoberg, 1988). The Arabian High intensification combined with the lower pressures in northeast Africa—due to a weakened Saharan High and the Sudanese Low—causes the isobars over the northern Red Sea to be across the central axis with geostrophic surface winds being parallel to them and blowing westward. The intensification of the Arabian High during large-scale westward wind events is robust. It appears in all different-period composites we produced and in the snapshot maps during the westward wind events, which suggests that an SLP-based gradient index between the Saudi Arabian Peninsula and northeast Africa could be used to monitor the westward wind/dry-air outbreak events. The schematic in Figure 20 summarizes our findings, which are distinct from the ARST systems that can also take place during the cool season. Compare Figure 20, for instance, with Figure 1 of de Vries et al. (2016) and Figures 15 of de Vries et al. (2013) and Dasari et al. (2018).

We notice several differences between the large-scale westward wind event and the wintertime severe heat loss SLP composite of Papadopoulos et al. (2013). This fact is not surprising since we have determined that only 6% of the severe heat loss days north of 25°N, defined according to Papadopoulos et al. (2013), are concurrent with westward wind events between 1980 and 2015. There are three significant differences between the composites. First, in the severe heat loss composite, the Azores High core is displaced eastward, over the Mediterranean Sea, while in the westward wind event composite, it is centered at about 30°W–35°N, over the Atlantic Ocean. Second, the anticyclone over Turkey (high SLP), well defined in the severe heat loss case at about 40°E–38°N, has no apparent signature in the westward wind event composite. Third, and likely the most critical difference, the tongue-like feature over the Arabian Peninsula associated with westward wind events is not present in the Papadopoulos et al. (2013) composite.

The SLP westward wind event composite over the Red Sea resembles the snapshot maps on the 14 January 2009 (Jiang et al., 2009, their Figure S1) and on 19 March 2012 (Prakash et al., 2015, their Figures 2c and 2f). Both events are associated with intense dust storms (Kalenderski et al., 2013; Prakash et al., 2015). The dust aerosols during the storms significantly reduce the solar radiation reaching the sea surface (Kalenderski et al., 2013). It is not a surprise that the SLP and the wind patterns that give rise to wintertime dust storms near the Red Sea eastern boundary are similar to the dry-air westward wind events presented in this paper. Jiang et al. (2009) have already shown that the westward winds can carry dust from the Arabian Desert, with the dust acting as a tracer of the surface winds in Moderate Resolution Imaging Spectroradiometer (MODIS) true-color images (see also Menezes et al., 2018, Figure 8).

An anti-cyclone (clockwise) circulation over most of the Arabian Peninsula exists in the westward wind event composites. This circulation, of which the northern Red Sea westward winds are part, is also characterized by intensified (8 m/s) and cold (10°C) southward surface winds over the Persian Gulf. These Gulf winds may coincide with Shamal events that bring cold and dry air over the Gulf, leading to excessive evaporation and severe heat loss by the sea (Al Senafi & Anis, 2015; El-Sabh & Murty, 1989; Perrone, 1979; Rao et al., 2001; Shi et al., 2004; Thoppil & Hogan, 2010). Aboobacker et al. (2011) describe a Shamal event on 2 February 2008, and their Figure 3d shows westward winds over the northern Sea concomitant with Shamal winds over the Gulf; both patterns also appear in the daily-mean MERRA-2 wind fields on that day. In Shi et al. (2004), the high SLP associated with Shamal winds on 28 January 1991 during Operation Desert Storm has a tongue-like high-SLP feature over the Arabian Peninsula that is similar to the westward wind event composites. Their map shows southward surface winds in the Gulf, the Shamal winds, and westward winds in the northern Red Sea, a pattern also reproduced by MERRA-2 on 28 January 1991. Hence, the winter Shamal winds in the Persian Gulf and the westward winds over the northern Red Sea are very likely to be part of the same subsynoptic-scale feature (a northward, enhanced Arabian High), a conjecture that needs further investigation.

A sudden blast of dry air accompanies westward wind events. The WHOI/KAUST mooring data show that the offshore relative humidity drops down to 30% during these events in contrast with the typical winter relative humidity of about 60%—precipitation is negligible during westward wind events. This dryness is because the westward winds are from the Arabian Desert. Abualnaja et al. (2015) and Bower and Farrar (2015) have already noted that the wind direction has a strong influence on the specific humidity over the Red Sea. As a consequence of their dryness and relatively cold temperatures, the westward winds cause a sharp increase in latent heat loss (evaporation) by the sea, which can reach 7 m/year. Their consequences are similar to cold air outbreaks occurring at midpolar and subpolar latitudes (e.g., Dorman et al., 2006; Lee et al., 2005; Poulain et al., 2001; Marshall et al., 2009). However, during the westward wind events, the major factors controlling the latent heat loss are the zonal wind speed and the relative humidity as revealed by the latent heat flux decomposition, each one accounting for about half of the observed heat loss. Thermal-related parameters (near-surface stability, air, and sea surface temperatures) are not important according to the in situ observations from the WHOI/KAUST mooring. Typically, the wind strength is responsible for most of the high evaporation rates of the northern Red Sea in winter aside from westward wind events. Because of these characteristics, we referred to these westward wind events as dry-air outbreaks.

Chiefly, the dry-air outbreaks impact the eastern Red Sea region between 22°N and 26°N, a region dominated by the convoluted northward-flowing surface EBC in winter (e.g., Bower & Farrar, 2015; Sofianos & Johns, 2003; Yao, Hoteit, Pratt, Bower, Kohl, et al., 2014; Yao, Hoteit, Pratt, Bower, Zhai, et al., 2014). In all westward wind event composites we produced, there is a high evaporation pool (latent heat loss) in this region that stands out. This high evaporation pool between 22°N and 26°N in the eastern Red Sea not only appears in the composite maps but it is also a conspicuous feature in the snapshots during westward wind events. In this region, westward wind events account for about 20% of the extreme heat loss (fifth percentile) between December and February in MERRA-2 (about 40% in the short-record in situ data). The surface EBC is part of the basin-scale vertical overturning circulation that leads to the formation of the intermediate-depth RSOW in the northern Red Sea (e.g., Papadopoulos et al., 2015; Zhai, Bower, et al., 2015).

Given the strength of the sea surface latent heat losses in westward wind events and knowing that the deepening of the mixed layer by buoyancy loss forms the RSOW in winter (e.g., Zhai, Bower, et al., 2015), we hypothesize that the dry-air outbreaks may act preconditioning the northern Red Sea for the RSOW formation through water mass transformation and mixed-layer deepening. Therefore, our results suggest that

these events might be a significant process for the thermohaline-driven Red Sea overturning circulation. How the westward wind/dry-air outbreak events affect the northern Red Sea and the EBC, in particular, constitute the next step in our research program.

Although we should interpret with caution climate variations longer than interannual in reanalysis due to an evolving observing system (Bosilovich et al., 2017), MERRA-2 indicates that the occurrence of the dry-air outbreak events has grown from 1980 to 2015. Besides this positive trend, MERRA-2 also shows decadal modulations and substantial interannual variability in the westward wind event frequency, which agrees with Menezes et al. (2018) who found high variability in the number of westward wind events from year to year based on the decade-long QuikSCAT data. Interannual variability also characterizes the winter Shamal winds in the Persian Gulf (Rao et al., 2001). Between 1980 and 2012, based on in situ observations, Al Senafi and Anis (2015) describe an increase in the frequency of winter Shamal winds (see their Figure 14b).

Evidence of long-term changes in the Middle East climate also exists, mainly connected with changes in the Siberian High (e.g., Hasanean et al., 2013). Hence, the positive trend in the frequency of Red Sea westward wind/dry-air outbreak detected in MERRA-2 does not appear spurious. In winter, Abualnaja et al. (2015) found that the North Atlantic Oscillation, the East Atlantic-West Russia (EA/WR) teleconnection pattern, and the interannual variability of the Indian monsoon regime are the primary drivers of climate variability surrounding the Red Sea. Because the onset of westward wind events seems to involve large-scale synoptic processes at midpolar and subpolar latitudes, we speculate that the North Atlantic Oscillation and the EA/WR may explain the interannual to long-term variations in the occurrence of the westward wind events. We notice that since 2004, the EA/WR is in a negative state according to the index produced by the National Weather Service/Center for Weather and Climate Prediction/National Oceanic and Atmospheric Administration. It is not yet know whether the climate modes control the frequency of westward wind events in the Red Sea and the winter Shamal in the Gulf, but this subject would be an excellent topic for future studies of the Middle East climate.

Appendix A: Latent Heat Flux Decomposition: Analytical Expressions for the Partial Derivative Terms

The analytical form for the partial derivatives in equation (6) are given by (see Appendix A from Bosilovich et al., 2017; Richter & Xie, 2008, for details):

$$\frac{\partial Q_l}{\partial SST} = Q_l \frac{\alpha(b/SST^2 - c/SST) - RH\left[b/(SST+S)^2 - c/(SST+S)\right]}{\alpha - RH}, \tag{A1}$$

$$\frac{\partial Q_l}{\partial S} = Q_l \frac{RH\left[b/(SST+S)^2 - c/(SST+S)\right]}{\alpha - RH}, \tag{A2}$$

$$\frac{\partial Q_l}{\partial RH} = -\frac{Q_l}{\alpha - RH}, \tag{A3}$$

$$\frac{\partial Q_l}{\partial W} = \frac{Q_l}{W}, \tag{A4}$$

$$\frac{\partial Q_l}{\partial C_e} = \frac{Q_l}{C_e}, \tag{A5}$$

$$\frac{\partial Q_l}{\partial \rho_a} = \frac{Q_l}{\rho_a}, \tag{A6}$$

and for the wind components

$$\frac{\partial Q_l}{\partial u} = Q_l \frac{u}{w^2}, \tag{A7}$$

$$\frac{\partial Q_l}{\partial v} = Q_l \frac{v}{w^2}, \tag{A8}$$

and α is given by

$$\alpha \equiv \exp\left\{\frac{b}{SST+S} - \frac{b}{SST} - c\ln\left(\frac{SST}{SST+S}\right)\right\}, \tag{A9}$$

with values of $b = 6,743.769$ and $c = 4.8451$ (Emanuel, 1994, page 116; eq. 4.4.13).

Acknowledgments
We thank the three anonymous reviewers and the associated editor who provided valuable comments that contributed to the improvement of the present paper. We wish to acknowledge the use of the Ferret program (NOAA/PMEL) and NCL (doi: 10.5065/D6WD3XH5) for analysis and graphics in this paper. We thanks Julie Hildebrandt for helping with the final manuscript version, Marcio Vianna for fruitful discussion about this work, and Stephen Swift for pointing out the long time series from Yenbo and Wejh at the National Climatic Data Center (NCDC/NOAA). We acknowledge the Global Modeling and Assimilation Office (GMAO) and the Goddard Earth Sciences Data and Information Services Center (GESDISC) for the dissemination of MERRA-2 reanalysis and the NCDC/NOAA for making the Global Surface Summary of the Day freely and easily available on the internet. MERRA-2 and QuikSCAT winds at 25 and 12.5 km data are available online (https://disc.gsfc.nasa.gov/datareleases/merra_2_data_release; www.remss.com/missions/qscat/; and https://podaac.jpl.nasa.gov, respectively). The in situ data from the WHOI/KAUST mooring is available at a WHOI repository (http://uop.whoi.edu/projects/kaust/form.php) and provided solely for academic and research purposes. The mooring data collected during the WHOI-KAUST collaboration was made possible by award USA00001, USA00002, and KSA00011 to the WHOI by the KAUST in the Kingdom of Saudi Arabia. This work was supported by NSF grant OCE-1435665 and NASA grant NNX14AM71G.

References

Aboobacker, V. M., Vethamony, P., & Rashmi, R. (2011). Shamal swells in the Arabian Sea and their influence along the west coast of India. *Geophysical Research Letters*, *38*, L03608. https://doi.org/10.1029/2010GL045736

Abualnaja, Y., Papadopoulos, V. P., Josey, S. A., Hoteit, I., Kontoyiannis, H., & Raitsos, D. E. (2015). Impacts of climate modes on air-sea heat exchange in the Red Sea. *Journal of Climate*, *28*, 2665–2681. https://doi.org/10.1175/JCLI-D-14-00379.1

Al Senafi, F., & Anis, A. (2015). Shamals and climate variability in the Northern Arabian/Persian Gulf from 1973 to 2012. *International Journal of Climatology*, *35*, 4509–4528. https://doi.org/10.1002/joc.4302

Awad, A. M., & Almazroui, M. (2016). Climatology of the winter Red Sea trough. *Atmospheric Research*, *182*, 20–29. https://doi.org/10.1016/j.atmosres.2016.07.019

Beal, L. M., Ffield, A., & Gordon, A. L. (2000). Spreading of Red Sea overflow waters in the Indian Ocean. *Journal of Geophysical Research*, *105*, 8549–8564. https://doi.org/10.1029/1999JC900306

Bosilovich, M. G., Lucchesi, R., & Suarez, M. (2016). MERRA-2: File specification: Global Modeling and Assimilation Office Note No. 9 (Version 1.1). Greenbelt, MD: National Aeronautics and Space Administration (NASA) Goddard Space Flight Center.

Bosilovich, M. G., Robertson, F. R., Takacs, L., Molod, A., & Mocko, D. (2017). Atmospheric water balance and variability in the MERRA-2 reanalysis. *Journal of Climate*, *30*, 1177–1196. https://doi.org/10.1175/JCLI-D-16-0338.1

Bower, A. S., & Farrar, J. T. (2015). Air-sea interaction and horizontal circulation in the Red Sea. In N. M. A. Rasul & I. C. F. Stewart (Eds.), *The Red Sea* (pp. 329–342). Berlin Heidelberg: Springer. https://doi.org/10.1007/978-3-662-45201-1_19

Brown, G. F., Schmidt, D. L., & Huffman Jr., A. C. (1989). Geology of the Arabian Peninsula; shield area of western Saudi Arabia (*resreport No. 560*). Reston, VA: U.S. Geological Survey. https://doi.org/10.3133/pp560A

Churchill, J. H., Lentz, S. J., Farrar, J., & Abualnajab, Y. (2014). Properties of Red Sea coastal currents. *Continental Shelf Research*, *78*, 51–61. https://doi.org/10.1016/j.csr.2014.01.025

Dasari, H. P., Attada, R., Knio, O., & Hoteit, I. (2017). Analysis of a severe weather event over Mecca, Kingdom of Saudi Arabia, using observations and high-resolution modelling. *Meteorological Applications*, *24*, 612–627. https://doi.org/10.1002/met.1662

Dasari, H. P., Langodan, S., Viswanadhapalli, Y., Vadlamudi, B. R., Papadopoulos, V. P., & Hoteit, I. (2018). ENSO influence on the inter-annual variability of the Red Sea convergence zone and associated rainfal. *International Journal of Climatology*, *38*, 761–775. https://doi.org/10.1002/joc.5208

Davis, S. R., Pratt, L. J., & Jiang, H. (2015). The Tokar Gap jet: Regional circulation, diurnal variability, and moisture transport based on numerical simulations. *Journal of Climate*, *28*, 5885–5907. https://doi.org/10.1175/JCLI-D-14-00635.1

de Vries, A. J., Feldstein, S. B., Riemer, M., Tyrlis, E., Sprenger, M., Baumgart, M., et al. (2016). Dynamics of tropical-extratropical interactions and extreme precipitation events in Saudi Arabia in autumn, winter and spring. *Quarterly Journal of the Royal Meteorological Society*, *142*, 1862–1880. https://doi.org/10.1002/qj.2781

de Vries, A. J., Ouwersloot, H. G., Feldstein, S. B., Riemer, M., El Kenawy, A. M., McCabe, M. F., & Lelieveld, J. (2018). Identification of tropical-extratropical interactions and extreme precipitation events in the Middle East based on potential vorticity and moisture transport. *Journal of Geophysical Research: Atmospheres*, *123*, 861–881. https://doi.org/10.1002/2017JD027587

de Vries, A. J., Tyrlis, E., Edry, D., Krichak, S. O., Steil, B., & Lelieveld, J. (2013). Extreme precipitation events in the Middle East: Dynamics of the active Red Sea trough. *Journal of Geophysical Research: Atmospheres*, *118*, 7087–7108. https://doi.org/10.1002/jgrd.50569

Dorman, C. E., Carniel, S., Cavaleri, L., Sclavo, M., Chiggiato, J., Doyle, J., et al. (2006). February 2003 marine atmospheric conditions and the bora over the northern Adriatic. *Journal of Geophysical Research*, *111*, C03S03. https://doi.org/10.1029/2005JC003134

Edson, J. B., Jampana, V., Weller, R. A., Bigorre, S., Plueddemann, A. J., Fairall, C. W., et al. (2013). On the exchange of momentum over the open ocean. *Journal of Physical Oceanography*, *43*, 1589–1610. https://doi.org/10.1175/JPO-D-12-0173.1

El-Sabh, M. I., & Murty, T. S. (1989). Storm surges in the Arabian Gulf. *Natural Hazards*, *1*, 371–385. https://doi.org/10.1007/BF00134834

Emanuel, K. A. (1994). *Atmospheric convection*. Oxford: Oxford University Press.

Eshel, G., & Heavens, N. (2007). Climatological evaporation seasonality in the northern Red Sea. *Paleoceanography*, *22*, PA4201. https://doi.org/10.1029/2006PA001365

Eshel, G., & Naik, N. H. (1997). Climatological coastal jet collision, intermediate water formation, and the general circulation of the Red Sea. *Journal of Physical Oceanography*, *27*, 1233–1257. https://doi.org/10.1175/1520-0485(1997)027<1233:CCJCIW>2.0.CO;2

Fairall, C. W., Bradley, E. F., Hare, J. E., Grachev, A. A., & Edson, J. B. (2003). Bulk parameterization of air-sea fluxes: Updates and verification for the COARE algorithms. *Journal of Climate*, *16*, 571–591. https://doi.org/10.1175/1520-0442(2003)016<0571:BPOASF>2.0.CO;2

Farrar, J. T., Lentz, S. J., Churchill, J. H., Bouchard, P. R., Smith, J. C., Kemp, J. N., et al. (2009). King Abdullah University of Science and Technology (KAUST) mooring deployment cruise and fieldwork reports. Woods Hole: Woods Hole Oceanographic Institution. https://doi.org/10.1575/1912/3012

Han, W., & McCreary, J. (2001). Modeling salinity distributions in the Indian Ocean. *Journal of Geophysical Research*, *206*, 859–877. https://doi.org/10.1029/2000JC000316

Hasanean, H., Almazroui, M., Jones, P., & Alamoudi, A. A. (2013). Siberian high variability and its teleconnections with tropical circulations and surface air temperature over Saudi Arabia. *Climate Dynamics*, *41*, 2003–2018. https://doi.org/10.1007/s00382-012-1657-9

Jiang, H., Farrar, J. T., Beardsley, R. C., Chen, R., & Chen, C. (2009). Zonal surface wind jets across the Red Sea due to mountain gap forcing along both sides of the Red Sea. *Geophysical Research Letters*, *36*, L19605. https://doi.org/10.1029/2009GL040008

Kalenderski, S., Stenchikov, G., & Zhao, C. (2013). Modeling a typical winter-time dust event over the Arabian Peninsula and the Red Sea. *Atmospheric Chemistry and Physics*, *13*, 1999–2014. https://doi.org/10.5194/acp-13-1999-2013

Katsaros, K. (2001). Evaporation and humidity (2nd ed.)., *Encyclopedia of ocean sciences* (pp. 324–331). Academic Press. https://doi.org/10.1016/B978-012374473-9.00068-0

Krichak, S. O., Alpert, P., & Krishnamurti, T. N. (1997a). Interaction of topography and tropospheric flow—A possible generator for the Red Sea trough? *Meteorology and Atmospheric Physics*, *63*, 149–158. https://doi.org/10.1007/BF01027381

Krichak, S. O., Alpert, P., & Krishnamurti, T. N. (1997b). Red Sea trough/cyclone development—Numerical investigation. *Meteorology and Atmospheric Physics*, *63*, 159–169. https://doi.org/10.1007/BF01027382

Krichak, S. O., Breitgand, J. S., & Feldstein, S. B. (2012). A conceptual model for the identification of active Red Sea trough synoptic events over the Southeastern Mediterranean. *Journal of Applied Meteorology and Climatology*, *51*, 962–971. https://doi.org/10.1175/JAMC-D-11-0223.1

Langodan, S., Cavaleri, L., Viswanadhapalli, Y., & Hoteit, I. (2015). Wind-wave source functions in opposing seas. *Journal of Geophysical Research: Oceans*, *120*, 6751–6768. https://doi.org/10.1002/2015JC010816

Lee, C. M., Askari, F., Book, J., Carniel, S., Cushman-Roisin, B., Dorman, C., et al. (2005). Northern Adriatic response to a wintertime bora wind events. *EOS Transactions, AGU*, *86*, 157–165. https://doi.org/10.1029/2005EO160001

Marshall, J., Ferrari, R., Forget, G., Maze, G., Andersson, A., Bates, N., et al. (2009). The climode field campaign: Observing the cycle of convection and restratification over the gulf stream. *Bulletin of the American Meteorological Society*, *90*, 1337–1350. https://doi.org/10.1175/2009BAMS2706.1

McCarty, W., Coy, L., Gelaro, R., Huang, A., Merkova, D., Smith, E. B., et al. (2016). MERRA-2 input observations: Summary and assessment (*NASA/TM2016-104606*). Greenbelt, MD: Report Series on Global Modeling and Data Assimilation.

McPhaden, M. J., Meyers, G., Ando, K., Masumoto, Y., Murty, V. S. N., Ravichandran, M., et al. (2009). RAMA: The research moored array for African-Asian-Australian monsoon analysis and prediction. *Bulletin of the American Meteorological Society*, *90*, 459–480. https://doi.org/10.1175/2008BAMS2608.1

Menezes, V. V., Farrar, J. T., & Bower, A. S. (2018). Westward mountain-gap wind jets of the northern Red Sea as seen by QuikSCAT. *Remote Sensing of Environment*, *209*, 677–699. https://doi.org/10.1016/j.rse.2018.02.075

NGDC (2006). National Geophysical Data Center. 2-minute Gridded Global Relief Data (ETOPO2) v2. National Geophysical Data Center, NOAA. https://doi.org/10.7289/V5J1012Q

Papadopoulos, V. P., Abualnaja, Y., Josey, S. A., Bower, A., Raitsos, D. E., Kontoyiannis, H., & Hoteit, I. (2013). Atmospheric forcing of the winter air-sea heat fluxes over the northern Red Sea. *Journal of Climate*, *593*, 1685–1701. https://doi.org/10.1175/JCLI-D-12-00267.1

Papadopoulos, V. P., Zhan, P., Sofianos, S. S., Raitsos, D. E., Qurban, M., Abualnaja, Y., et al. (2015). Factors governing the deep ventilation of the Red Sea. *Journal of Geophysical Research: Oceans*, *120*, 7493–7505. https://doi.org/10.1002/2015JC010996

Pedgley, D. E. (1966). The Red Sea convergence zone. Part I—The horizontal pattern of winds. *Weather*, *21*, 350–358. https://doi.org/10.1002/j.1477-8696.1966.tb02776.x

Perrone, T. J. (1979). Winter shamal in the Persian Gulf (*TR 79-06*). Monterey, California: Naval Environmental Prediction Research Facility.

Poulain, P. M., Kourafalou, V. H., & Cushman-Roisin, B. (2001). Northern Adriatic sea. In B. Cushman-Roisin, M. Gacic, P. M. Poulain, & A. Artegiani (Eds.), *Physical oceanography of the Adriatic sea* pp. 143–165). Dordrecht: Springer. https://doi.org/10.1007/978-94-015-9819-4_5

Prakash, P. J., Stenchikov, G., Kalenderski, S., Osipov, S., & Bangalath, H. (2015). The impact of dust storms on the Arabian Peninsula and the Red Sea. *Atmospheric Chemistry and Physics*, *15*, 199–222. https://doi.org/10.5194/acp-15-199-2015

Rao, P. G., Al-Sulaiti, M., & Al-Mulla, A. H. (2001). Winter shamals in Qatar, Arabian Gulf. *Weather*, *56*, 444–451. https://doi.org/10.1002/j.1477-8696.2001.tb06528.x

Richter, I., & Xie, S. P. (2008). Muted precipitation increase in global warming simulations: A surface evaporation perspective. *Journal of Geophysical Research*, *113*, D24118. https://doi.org/10.1029/2008JD010561

Rienecker, M. M., Suarez, M. J., Gelaro, R. G., Todling, R., Bacmeister, J., Liu, E., et al. (2011). MERRA: NASA's Modern-Era Retrospective Analysis for Research and Applications. *Journal of Climate*, *24*, 3624–3648. https://doi.org/10.1175/JCLI-D-11-00015.1

Roberts, J. B., Robertson, F. R., Clayson, C. A., & Bosilovich, M. (2012). Characterization of turbulent latent and sensible heat flux exchange between the atmosphere and ocean in MERRA. *Journal of Climate*, *25*, 821–837. https://doi.org/10.1175/JCLI-D-11-00029.1

Roman, R. E., & Lutjeharms, J. R. E. (2007). Red sea intermediate water at the agulhas current termination. *Deep Sea Research Part I*, *54*, 1329–1340. https://doi.org/10.1016/j.dsr.2007.04.009

Roman, R. E., & Lutjeharms, J. R. E. (2009). Red Sea intermediate water in the source regions of the Agulhas Current. *Deep Sea Research Part I: Oceanographic Research Papers*, *56*, 939–962. https://doi.org/10.1016/j.dsr.2009.01.003

Shentsis, I., Laronne, J. B., & Alpert, P. (2012). Red Sea trough flood events in the Negev, Israel (1964–2007). *Hydrological Sciences Journal*, *57*, 42–51. https://doi.org/10.1080/02626667.2011.636922

Shi, J. J., Chang, S. W., Holt, T., Hogan, T. F., & Westphal, D. L. (2004). A meteorological reanalysis for the 1991 Gulf War. *Monthly Weather Review*, *132*, 623–640. https://doi.org/10.1175/1520-0493(2004)132<0623:AMRFTG>2.0.CO;2

Smith, W. H. F., & Sandwell, D. T. (1997). Global seafloor topography from satellite altimetry and ship depth soundings. *Science*, *277*, 1956–1962. https://doi.org/10.1126/science.277.5334.1956

Sofianos, S. S., & Johns, W. E. (2003). An Oceanic General Circulation Model (OGCM) investigation of the Red Sea circulation: 2. Three-dimensional circulation in the Red Sea. *Journal of Geophysical Research*, *108*(C3), 3066. https://doi.org/10.1029/2001JC001185

Sofianos, S. S., & Johns, W. E. (2015). Water mass formation, overturning circulation, and the exchange of the Red Sea with the adjacent basins. In N. M. A. Rasul, & I. C. F. Stewart (Eds.), *The Red Sea*. Berlin Heidelberg: Springer, pp. 343–353. https://doi.org/10.1007/978-3-662-45201-1_20

Sofianos, S. S., Johns, W. E., & Murray, S. P. (2002). Heat and freshwater budgets in the Red Sea from direct observations at Bab el Mandeb. *Deep-Sea Research Part II: Topical Studies in Oceanography*, *49*, 1323–1340. https://doi.org/10.1016/S0967-0645(01)00164-3

Stiles, B., Fore, A. G., Strub, P. T., & James, C. (2017). QuikSCAT coastal wind products. NASA OVWST and International OVWST Meeting 2017.

Swift, S. A., & Bower, A. S. (2003). Formation and circulation of dense water in the Persian/Arabian Gulf. *Journal of Geophysical Research*, *108*(C1), 3004. https://doi.org/10.1029/2002JC001360

Thoppil, P. G., & Hogan, P. J. (2010). Persian Gulf response to a wintertime shamal wind events. *Deep-Sea Research I*, *8*, 946–955. https://doi.org/10.1016/j.dsr.2010.03.002

Tragou, E., Garrett, C., Outerbridge, R., & Gilman, C. (1999). The heat and freshwater budgets of the Red Sea. *Journal of Physical Oceanography*, *29*, 2504–2522. https://doi.org/10.1175/1520-0485(1999)029<2504:THAFBO>2.0.CO;2

Tsvieli, Y., & Zangvil, A. (2005). Synoptic climatological analysis of wet and dry Red Sea troughs over Israel. *International Journal of Climatology*, *25*, 1997–2015. https://doi.org/10.1002/joc.1232

Tsvieli, Y., & Zangvil, A. (2007). Synoptic climatological analysis of Red Sea trough and non-Red Sea trough rain situations over Israel. *Advanced Geosciences*, *12*, 137–143. https://doi.org/10.5194/adgeo-12-137-2007

Vimont, D., Alexander, M., & Fontaine, A. (2009). Midlatitude excitation of tropical variability in the Pacific: The role of thermodynamic coupling and seasonality. *Journal of Climate*, *22*, 518–534. https://doi.org/10.1175/2008JCLI2220.1

Viswanadhapalli, Y., Dasari, H. P., Langodan, S., Challa, V. S., & Hoteit, I. (2017). Climatic features of the Red Sea from a regional assimilative models. *International Journal of Climatology*, *37*, 2563–2581. https://doi.org/10.1002/joc.4865

Vojtesak, M. J., Martin, K. P., Myles, G., & Gilford, M. T. (1991). SWANEA (Southwest Asia-Northeast Africa): A climatological study. Volume 2. The Middle East Peninsula (*USAFETA/TN-91/002*). Scott Air Force Base, Illinois: Air Force Environmental Technical Applications Center.

Vorhees, D. C. (2006). *The impacts of Global Scale Climate Variations on Southwest Asia*. Monterey, California: Naval Postgraduate School. http://hdl.handle.net/10945/2946

Wafar, M., Ashraf, M., Manikandan, K., Qurban, M., & Kattan, Y. (2016). Gulf of Aden Intermediate Water (GAIW) in the Red Sea. *Journal of Marine Systems*, *154*, 243–251. https://doi.org/10.1016/j.jmarsys.2015.10.016

Walters, K. R., & Sjoberg, W. F. (1988). The Persian Gulf region—A climatological study (*USAFETAC/TN-88/002*). Scott Air Force Base, Illinois: Air Force Environment Technical Applications Center.

Yao, F., Hoteit, I., Pratt, L. J., Bower, A. S., Kohl, A., Gopalakrishnan, G., & Rivas, D. (2014). Seasonal overturning circulation in the Red Sea: 2. Winter circulation. *Journal of Geophysical Research: Oceans*, *119*, 2263–2289. https://doi.org/10.1002/2013JC009331

Yao, F., Hoteit, I., Pratt, L. J., Bower, A. S., Zhai, P., Kohl, A., & Gopalakrishnan, G. (2014). Seasonal overturning circulation in the Red Sea: 1. Model validation and summer circulation. *Journal of Geophysical Research: Oceans*, *119*, 2238–2262. https://doi.org/10.1002/2013JC009004

You, Y. (1998). Intermediate water circulation and ventilation of the Indian Ocean derived from water-mass contributions. *Journal of Marine Research*, *56*, 1029–1067. https://doi.org/10.1357/002224098765173455

Yu, L., Jin, X., Josey, S. A., Lee, T., Kumar, A., Wen, C., & Xue, Y. (2017). The global ocean water cycle in atmospheric reanalysis, satellite, and ocean salinity. *Journal of Climate*, *30*, 3829–3852. https://doi.org/10.1175/JCLI-D-16-0479.1

Yu, L., Jin, X., & Weller, R. A. (2008). Multidecade global flux datasets from the Objectively Analyzed Air-sea Fluxes (OAFlux) Project: Latent and sensible heat fluxes, ocean evaporation, and related surface meteorological variables (*OA-2008-01*). Woods Hole, Massachusetts: Woods Hole Oceanographic Institution.

Zarokanellos, N. D., Kurten, B., Churchill, J. H., Roder, C., Voolstra, C. R., Abualnaja, Y., & Jones, B. H. (2017). Physical mechanisms routing nutrients in the central Red Sea. *Journal of Geophysical Research: Oceans*, *122*, 9032–9046. https://doi.org/10.1002/2017JC013017

Zarokanellos, N. D., Papadopoulos, V. P., Sofianos, S. S., & Jones, B. H. (2017). Physical and biological characteristics of the winter-summer transition in the Central Red Sea. *Journal of Geophysical Research: Oceans*, *122*, 6355–6370. https://doi.org/10.1002/2017jc012882

Zhai, P., Bower, A. S., Smethie, W., & Pratt, L. (2015). Formation and spreading of Red Sea outflow water in the Red Sea. *Journal of Geophysical Research: Oceans*, *120*, 6542–6563. https://doi.org/10.1002/2015JC010751

Zhai, P., Pratt, L. J., & Bower, A. (2015). On the crossover of boundary currents in an idealized model of the Red Sea. *Journal of Physical Oceanography*, *45*, 1410–1425. https://doi.org/10.1175/JPO-D-14-0192.1

Zolina, O., Dufour, A., Gulev, S., & Stenchikov, G. (2017). Regional hydrological cycle over the Red Sea in ERA-Interim. *Journal of Hydrometeorology*, *18*, 65–83. https://doi.org/10.1175/JHM-D-16-0048.1